CrossMark

Spectral Energy Distributions for 258 Local Volume Galaxies

Daniel A. Dale[1] , Médéric Boquien[2] , Jordan A. Turner[1,3] , Daniela Calzetti[4] , Robert C. Kennicutt, Jr.[5,6] , and Janice C. Lee[7]

[1] Department of Physics and Astronomy, University of Wyoming, Laramie, WY 82071, USA; ddale@uwyo.edu
[2] Centro de Astronomía (CITEVA), Universidad de Antofagasta, Avenida Angamos 601, Antofagasta, Chile
[3] The Aerospace Corporation, El Segundo, CA, 90245, USA
[4] Department of Astronomy, University of Massachusetts, Amherst, MA 01002, USA
[5] Department of Astronomy and Steward Observatory, University of Arizona, Tucson, AZ 85721, USA
[6] Department of Physics and Astronomy, Texas A&M University, College Station, TX 77843, USA
[7] Gemini Observatory/NSFŽ019s NOIRLab, 950 N. Cherry Avenue, Tucson, AZ 85719, USA

Abstract

We present model spectral energy distribution (SED) fits to ultraviolet/optical/infrared observations for the 258 nearby galaxies in the Local Volume Legacy survey, a sample dominated by lower-luminosity dwarf irregular systems. The data for each galaxy include up to 26 spatially-integrated broadband and narrowband fluxes from the Galaxy Evolution Explorer, Spitzer Space Telescope, and Infrared Astronomical Satellite space-based platforms, and from the Sloan Digital Sky Survey, Two Micron All Sky Survey, and other ground-based efforts. The CIGALE SED fitting package is employed using a delayed star-formation history with an optional late burst or quenching episode to constrain 11 different free parameters that characterize the properties of each galaxy's stellar and dust emission, with the overriding constraint that the ultraviolet/optical emission absorbed by interstellar dust grains is emitted in equal energy portions at infrared wavelengths. The main results are: (i) 94% of the SED fits yield reduced χ^2 values less than 3; (ii) the modeled stellar masses agree with those derived from 3.6 μm-based measures with a scatter of 0.07 dex; (iii) for a typical galaxy in the sample the SED-derived star-formation rate averaged over the past 100 Myr is about 88% of the value derived from standard hybrid indicators on similar timescales; and (iv) there is a statistically significant inverse relation between the stellar mass fraction appearing in the late burst and the total stellar mass. These results build upon prior SED modeling efforts in the local volume and lay the groundwork for future studies of more distant low-metallicity galaxies with JWST.

Unified Astronomy Thesaurus concepts: Galaxies (573); Spectral energy distribution (2129)

Supporting material: machine-readable tables

1. Introduction

Understanding the interplay between star formation and the interstellar medium within galaxies has long been a primary goal of galaxy evolution studies. However, while the broad brush strokes of star formation have come into focus over the past decades, many details remain to be filled in. Infrared studies of nearby galaxies provide a two-fold advantage to understanding the processes that underlie the evolution of star formation and the interstellar medium: enhanced spatial resolution and the ability to penetrate much of the gas and dust that otherwise obscure ultraviolet and optical observations. Several studies of relatively large samples of nearby galaxies have utilized space-based infrared observatories, e.g., the Spitzer Nearby Galaxies Survey (SINGS; Kennicutt et al. 2003), the Great Observatories All-Sky LIRG Survey (Armus et al. 2009), the Spitzer Survey of Stellar Structure in Galaxies (Sheth et al. 2010), Key Insights on Nearby Galaxies: A Far-Infrared Survey with Herschel (KINGFISH; Kennicutt et al. 2011), the Dwarf Galaxy Survey (DGS; Madden et al. 2013), and A Survey of Far-Infrared Lines in Nearby Galaxies (Herrera-Camus et al. 2018). However, none of these surveys provides a statistically representative survey of the population of galaxies found in the local volume. Most of these efforts are biased toward massive, metal-rich, and high-surface-brightness systems. The sampling that does exist for lower-mass systems is sparse, and is far from representative, despite the fact that this population offers the greatest diversity of properties, the best-measured star-formation histories, and hence optimal leverage for elucidating the processes that underlie star formation and shape the properties of galaxies.

The Local Volume Legacy (LVL) survey has provided an unbiased, fully representative, and statistically robust sample of nearby star-forming galaxies. The overarching goal of the LVL survey has been to provide critical insight into two of the primary processes that shape the growth of galaxies: star formation and its interaction with the interstellar medium. In a series of papers the LVL team has investigated the spatially-resolved star formation, dust, and red stellar populations of local galaxies that span the full diversity of luminosities, surface brightnesses, metallicities, dust characteristics, and star-formation properties (e.g., Lee et al. 2009b; Boquien et al. 2010; Calzetti et al. 2010; Marble et al. 2010; Bothwell et al. 2011; Berg et al. 2012; Weisz et al. 2012; Grasha et al. 2013; Cook et al. 2014a, 2016). The tiered survey includes: (1) all known galaxies inside a subvolume bounded by 3.5 Mpc, and (2) an unbiased sample of galaxies within the larger, and more representative, 11 Mpc sphere. This strategy provides volume-complete coverage of galaxies over the entire luminosity function, with the minimum sample needed to fully

characterize the local galaxy population. The data backbone of the LVL survey has been the Galaxy Evolution Explorer (GALEX), Hα narrowband, and Spitzer Space Telescope imaging obtained for the volume-complete sample. Additional broadband optical and infrared observations have been obtained or compiled to complete the panchromatic census.

In this paper we utilize the CIGALE software package to fit the multiwavelength data set to constrain the physical properties and star-formation histories of the LVL sample. Janowiecki et al. (2017) previously explored spectral energy distribution (SED) fitting of the LVL sample in the context of using it as a reference sample for their study of 18 blue compact dwarf galaxies. Janowiecki et al. (2017) used CIGALE to fit the LVL SEDs, utilizing 14 different broadband fluxes from GALEX FUV/NUV, $UBVR_C I_C$, 2MASS JHK_s, Spitzer IRAC, and Spitzer MIPS 24 μm. Their main finding was no surprise: compared to the overall dwarf galaxy population, blue compact dwarf galaxies are currently undergoing extreme star-formation episodes, as quantified by the relative masses and amplitudes of the starbursts. We expand beyond the work of Janowiecki et al. (2017) by including up to 26 fluxes for the LVL sample—the fluxes employed in Janowiecki et al. (2017) plus Hα narrowband, SDSS ugriz, Spitzer MIPS 70 and 160 μm, and IRAS broadband fluxes, where available. In addition, our fits utilize the Draine et al. (2014) dust emission models instead of the one-parameter dust models of Dale et al. (2014), so we are able to report physical properties of the dust population such as the dust mass fraction that is locked up in polycyclic aromatic hydrocarbons (PAHs). We also use a "delayed" star-formation model with the possibility of a late quenching or burst episode, whereas they used an exponentially-decaying SFH with an exponentially-decaying late burst. Finally, Janowiecki et al. (2017) only reported the fit parameters for their sample of 18 blue compact dwarf galaxies; we report here the fit parameters for the larger LVL sample.

Section 2 summarizes the sample of galaxies studied in this effort. Section 3 reviews and presents the multiwavelength data set used here, and the analysis of the data is presented in Section 4. Section 5 presents the main results, and Section 6 provides concluding remarks.

2. Sample

The LVL sample of 258 galaxies is fully described in Dale et al. (2009). Briefly, the sample has a two-fold lineage that derives from the "ANGST" ACS Nearby Galaxy Survey Treasury (Dalcanton et al. 2009) and the "11HUGS" 11 Mpc Hα and Ultraviolet Survey (Kennicutt et al. 2008; Lee et al. 2009b). ANGST is a volume-limited survey beyond the Local group that reaches out to 3.5 Mpc and additionally samples the M 81 group and Sculptor filament. The 11HUGS sample targeted star-forming disk galaxies out to $D \leqslant 11$ Mpc that met the criterion $m_B < 15$ mag. Both of these surveys avoid the Galactic plane, with the criterion for ANGST satisfying $|b| > 20°$ and that for 11HUGS following $|b| > 30°$. Figure 1 demonstrates the sample's range of star-formation rates and stellar masses based on 3.6 μm luminosities. Clearly this volume-limited survey provides a different sampling of the galaxy population than traditional notions of the "red sequence" and "blue cloud;" a large fraction of the LVL sources skews to much smaller stellar masses and star-formation rates than the bulk of the 15,750 objects in the "z0MGS" $z = 0$ Multiwavelength Galaxy Synthesis catalog of

nearby ($\lesssim 50$ Mpc) galaxies (Leroy et al. 2019). In fact, the z0MGS sample targets galaxies more luminous than the Large Magellanic Cloud (LMC) by adopting a luminosity cut of $M_B < -18$ mag and 81% of the LVL sample is less luminous than the LMC (Dale et al. 2009). If we define a dwarf galaxy as having a stellar mass less than $10^9 M_\odot$, then 75% of the LVL sample is populated by dwarf systems. This deviation of the LVL sample from the red-and-dead and main-sequence norms is reflected in the distribution of optical morphologies: the sample is comprised of 8%, 31%, and 60% early-type/lenticular, spiral, and irregular galaxies, respectively.

The median distance for the sample is 5.9 Mpc. The majority of the distances lie between 0.5 Mpc and 11 Mpc, with outliers being the Magellanic Clouds (50–60 kpc), UGC 06782 (14 Mpc), IC 2049 (17 Mpc), and UGC 07321 (20 Mpc). Most of the distances derive from either tip of the red-giant-branch measurements (39.9%) or from flow-corrected velocities (35.3%). The distance estimates for the remaining galaxies derive from an assortment of techniques including the luminosity of the brightest stars (13.2%), Cepheid observations (6.2%), surface brightness fluctuations (3.1%), membership in a known galaxy group (1.6%), and the Tully-Fisher relation (0.8%). Additional details on the galaxy distances may be found in Dale et al. (2009).

3. Data

The LVL broadband data sets used in this work include GALEX ultraviolet (Lee et al. 2011), 2MASS near-infrared (Dale et al. 2009), and Spitzer infrared imaging (Dale et al. 2009). We also utilize the spatially-integrated optical broadband flux densities provided by Cook et al. (2014b), who use the same photometric apertures as in Dale et al. (2009; see also Dale et al. 2007, 2012, 2017). As explained in Dale et al. (2009): (i) the photometric apertures have been carefully crafted to capture all of the observable emission, (ii) the apertures are the same across all optical/infrared wavelengths, and (iii) the appropriate aperture corrections have been applied at each wavelength. Additional standard corrections to the flux densities used in the SED fitting, e.g., removing the local "sky"/foreground stars/background galaxies and correcting for foreground Milky Way extinction, have been applied as well.[8] We have supplemented these data sets with global IRAS infrared flux densities taken from Rice et al. (1988), Moshir et al. (1990), Sanders et al. (2003), and our own extractions using the IRAS Scan Processing and Integration Tool.[9] The majority of the LVL galaxies have infrared surface brightnesses that are too faint for secure IRAS detections; including our own SCANPI-based extractions for [6, 8, 23, 23] LVL galaxies with no published IRAS measurements, we have global IRAS flux densities for [61, 70, 125, 119] galaxies, respectively, for the IRAS [12 μm, 25 μm, 60 μm, 100 μm] filters. A comparison of the 8 new SCANPI-based IRAS 25 μm fluxes with the corresponding Spitzer 24 μm fluxes shows a median flux ratio of $f_\nu(25 \mu m)/f_\nu(24 \mu m) = 1.2$ and a dispersion of 0.1 dex. The major axes of these 23 galaxies with new SCANPI-based IRAS fluxes are all larger than the angular resolution of IRAS. Finally, we include integrated Hα fluxes that are corrected for N II emission from Kennicutt et al. (2008). The table of

---

[8] However, we point out that the fluxes provided in the Appendix are not corrected for Milky Way foreground extinction.
[9] https://irsa.ipac.caltech.edu/IRASdocs/scanpi_over.html
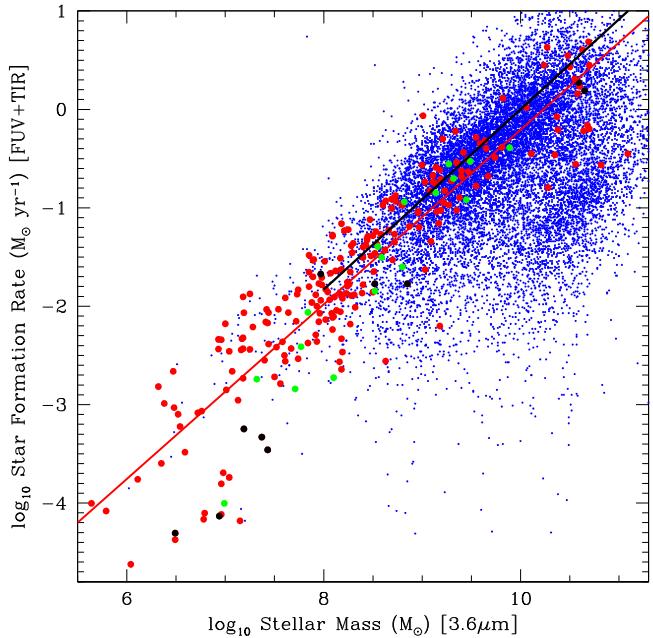
Figure 1. Comparison of global star-formation rates and stellar masses for the LVL sample (filled red/black/green circles) with the "z0MGS" $z = 0$ Multiwavelength Galaxy Synthesis catalog (blue dots) of Leroy et al. (2019). The star-forming main-sequence linear relation from Peng et al. (2010) is shown as a black line; our best-fit relation for the LVL sample is provided as a red line. LVL star-formation rates are based on the Hao et al. (2011) FUV+TIR calibrations for 216 galaxies (red circles), the Hao et al. (2011) NUV+TIR calibrations for 11 galaxies without (GALEX) FUV observations (black circles), and the Kennicutt et al. (2009) Hα+24 μm calibration for 17 galaxies with neither (GALEX) NUV nor FUV observations (green circles). Stellar masses are based on 3.6 μm fluxes using the prescription outlined in Appendix A.4 of Leroy et al. (2019).

Table 1
Detections and Upper Limits by Wavelength

Telescope	Filter	λ (μm)	# Detections	# Upper Limits
GALEX	FUV	0.15	222	0
GALEX	NUV	0.23	233	0
multiple	U	0.36	132	0
multiple	B	0.44	185	0
multiple	V	0.55	129	0
multiple	R_C	0.71	188	0
SDSS	u	0.29	144	1
SDSS	g	0.48	146	0
SDSS	r	0.62	146	0
SDSS	i	0.76	146	0
SDSS	z	0.91	146	0
2MASS	J	1.24	229	26
2MASS	H	1.66	228	27
2MASS	K_s	2.16	219	36
Spitzer	IRAC1	3.6	247	9
Spitzer	IRAC2	4.5	247	10
Spitzer	IRAC3	5.8	212	43
Spitzer	IRAC4	8.0	214	43
Spitzer	MIPS1	24	210	47
Spitzer	MIPS2	70	204	53
Spitzer	MIPS3	160	198	59
IRAS	IRAS1	12	61	0
IRAS	IRAS2	25	70	0
IRAS	IRAS3	60	125	0
IRAS	IRAS4	100	119	0
multiple	Hα	0.6563	218	6

photometry is provided in the Appendix. Table 1 provides the number of available detections as well as the number of upper limits for each of the 26 wavelengths employed here for the overall sample of 258 LVL galaxies. The treatment of upper limits in the SED fitting is described in Section 4.3 of Boquien et al. (2019), which follows from the technique laid out in Appendix A2 of Sawicki (2012). The upper limits and less secure photometry are limited to low-mass galaxies; 91% (100%) of the upper limits correspond to galaxies with $\log_{10} M_*/M_\odot \lesssim 8.0$ (8.7).

4. Spectral Energy Distribution Fits

We employ the CIGALE spectral energy distribution fitter (Boquien et al. 2019) to constrain several physical parameters that characterize the stellar and dust properties in the LVL galaxies. CIGALE functions on a principle of energy balance, whereby the (primarily) ultraviolet and optical stellar emission that is absorbed by interstellar dust grains reappears in the infrared in energetically equal amounts in the form of dust continuum(s) and PAH feature emission (see also, e.g., da Cunha et al. 2008; Leja et al. 2017). Both nebular and synchrotron emission are also modeled in CIGALE. Our adoptions include the stellar and dust emission libraries of Bruzual & Charlot (2003) and Draine et al. (2014), the Chabrier (2003) stellar initial mass function, and a dust attenuation curve based on Calzetti et al. (2000) and Leitherer et al. (2002). The grid values for each parameter in the fits are listed in Table 2. The total number of grid points (or different

models) is
$4 \times 7 \times 5 \times 14 \times 18 \times 3 \times 18 \times 6 \times 9 \times 3 \times 11 = 3.4 \times 10^9$.

We follow Hunt et al. (2019) and opt for a "delayed" star-formation history with the option for an additional late burst or quenching of the star formation that begins at time t_{bq}, also known as the `sfhdelayedbq` module within CIGALE:

$$\mathrm{SFR}(t) \propto \begin{cases} t \exp(-t/\tau_{main}), & t \leqslant t_{bq} \\ r_{SFR}\, \mathrm{SFR}(t = t_{bq}), & t > t_{bq}. \end{cases} \quad (1)$$

Previous CIGALE-based efforts for samples of nearby star-forming galaxies have shown that there are minimal differences ($\sim$0.1 dex) in the output fit values when using a delayed exponential + late burst star-formation history versus using a purely exponentially-decaying + late burst (Dale et al. 2016; Salim et al. 2016). However, we find here for the LVL sample that implementing a late burst/quench using the `sfhdelayedbq` CIGALE module provides superior SED fits (i.e., lower $\chi^2_{reduced}$) than when invoking the `sfhdelayed` module with a late burst option. The latter module yields poor fits in the ultraviolet wavelength range for about a third of the LVL sample, which results in SED-based star-formation rates and stellar masses that are in poor agreement with those derived by independent measures that are not based on SED fits (see Section 4). Two of the parameters relevant to our adopted star-formation history are the age and e-folding time τ_{main} of the main stellar population. The onset age for the main stellar population is fixed to 13 Gyr but the results of this work are insensitive to values tested between 10 and 13 Gyr. We also model a possible late quenching or burst event via its age (t_{bq} in

Table 2
CIGALE SED Fit Parameters

Parameter	Notation	Allowed Values
bc03 Bruzual & Charlot (2003) stellar library		
Metallicity	metallicity	0.004, 0.008, 0.02, 0.05
Initial mass function	imf	1 (Chabrier 2003)
sfhdelayedbq delayed star-formation history with optional constant burst/quench		
e-folding time of the main population (Gyr)	tau_main	1, 2, 3, 4, 5, 7.5, 10
Age of oldest stars (Gyr)	age_main	13
Age of the burst/quench episode (Myr)	age_bq	10, 25, 50, 75, 100
Ratio of the SFR after/before age_bq	r_sfr	0, 0.2, 0.4, 0.6, 0.8, 1, 1.25, 1.5, 1.75, 2, 2.5, 5, 7.5, 10
nebular nebular emission		
Ionization parameter	logU	−3.0
Electron density (cm^{-3})	n_e	100
Lyman continuum escape fraction	f_esc	0.0
Lyman continuum dust absorption fraction	f_dust	0.0
Emission line width ($km\ s^{-1}$)	lines_width	300
dustatt_modified_starburst attenuation curve		
Color excess for nebular emission	E_BV_lines	0.01,0.02,0.04,0.06,0.08,0.1,0.15,0.2,0.25,0.3,0.35,0.4,0.5,0.6,0.7,0.8,0.9,1
Reduction factor applied to E_BV_lines for stellar $E(B-V)$	E_BV_factor	0.25, 0.50, 0.75
UV bump amplitude	uv_bump_amplitude	0
Slope δ of power law that modifies attenuation curve	powerlaw_slope	$[-1.5, 0.2]$ with spacings of 0.1
dl2014 dust emission		
PAH dust mass fraction q_{PAH}	qpah	0.47, 1.12, 2.50, 3.90, 5.26, 6.63
Minimum radiation field U_{min}	umin	0.1, 0.25, 0.50, 1.0, 2.5, 5.0, 10.0, 25.0, 50.0
Power-law slope $dM_{dust}/dU \propto U^{-\alpha}$	alpha	1.5, 2.0, 2.5
Illumination fraction from U_{min} to U_{max}	gamma	$[10^{-3}, 10^{-0.5}]$ with spacings of 0.25 dex

Equation (1) is when the burst/quench turns on; age_bq in Table 2 is the duration of the burst/quenching) and a multiplicative amplitude r_{SFR} that applies instantaneously at the time of the burst / quenching event (see Boquien et al. 2019 for details). Though it is tempting to tailor the star-formation history separately for different galaxy bins (e.g., optical morphology or stellar mass), for ease of comparison we adopt the same star-formation history for all galaxies and assume identical grid values for each SED fit.

The modeled attenuation curve allows for ranges in the color excess for both nebular line and stellar continuum emission and the slope δ of a power law that modifies the curve. The UV "bump" amplitude is fixed to be zero. The properties of the dust emission that are allowed to vary include the PAH mass fraction q_{PAH}, the minimum intensity U_{min} of the radiation field that illuminates the dust, and the fraction of the dust mass γ that is associated with the power-law (i.e., nondiffuse) part of the starlight intensity distribution (see Draine et al. 2014). Nebular emission is included in the spectral energy distribution fits, with the chosen (fixed) parameter values as listed in Table 2. The output parameter values and uncertainties from the spectral energy distribution fits come in two flavors: a "best-fit" solution via a χ^2 minimization as well as a Bayesian-like approach that provides output based on a likelihood-weighting scheme involving the χ^2 value for each model grid point (Section 4.4 of Boquien et al. 2019). In almost all cases we utilize the fit values derived from the more robust Bayesian-based process,

in order to avoid the limitations imposed by the discreteness of the grid-based best-fit solutions (Taylor et al. 2011).

The resulting SED fit parameter values are presented in the Appendix for each galaxy. For galaxies without secure MIPS 70 μm and 160 μm detections, we provide dust mass upper limits as the sum of the SED-derived dust mass plus its Bayesian uncertainty. Accordingly, for these galaxies the interpretation of the other dust-related parameters is limited.

5. Results

Figure 2 provides example CIGALE spectral energy distribution fits for two low-luminosity irregulars and one massive spiral galaxy in the LVL sample. The differences between the observed and intrinsic ultraviolet/optical spectra are due to absorption by dust and are equal in energy to that emitted by dust in the infrared, as prescribed by design in the fitting code. The faintest target of these three example galaxies, UGC 6900, lacks infrared detections at wavelengths longward of 24 μm (see Table 1) and thus the SED fit for this lower-luminosity galaxy relies on a more limited wavelength range than do the fits for NGC 4214 and NGC 3031 (we have incorporated the flux upper limits in our CIGALE SED fitting). The reduced χ^2 values for these three example cases are all less than unity.

The top panel in Figure 3 displays $\chi^2_{reduced}$ for the entire sample as a function of total SED-derived stellar mass. There is a trend with lower-mass (fainter) galaxies having larger $\chi^2_{reduced}$, as expected (the Spearman's rank correlation
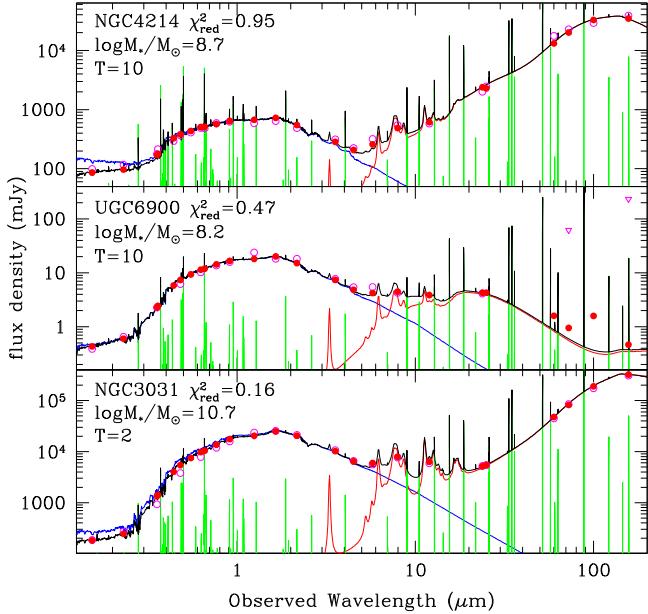
Figure 2. Example CIGALE fits for three LVL galaxies, one a massive spiral galaxy (NGC 3031 = M 81) and two lower-luminosity irregular galaxies (NGC 4214 and UGC 6900). The blue, red, green, and black lines represent the intrinsic stellar continuum, dust continuum, nebular, and total modeled emission, respectively. The filled red circles represent the model flux densities in the 25 possible broadband bandpasses whereas the open magenta circles are the observed flux densities (upper limits are open magenta triangles).
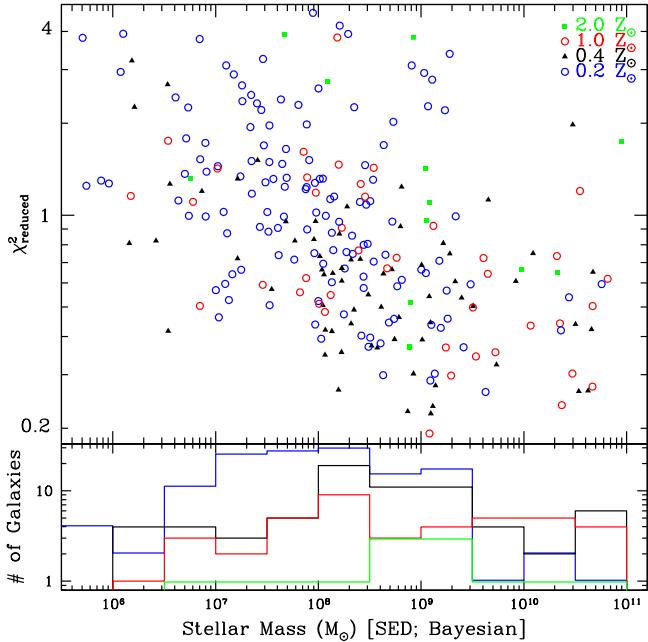

Figure 3. Top: the reduced χ^2 values as a function of SED-derived stellar mass. The points are color coded according to best-fit stellar metallicity. Bottom: The distributions of the best-fit metallicities as a function of stellar mass using the same color scheme as in the top panel.

coefficient is -0.51). The histograms in the bottom panel of Figure 3 support a scenario of higher best-fit metallicities for more massive galaxies, also in agreement with expectations (e.g., Tremonti et al. 2004). The median $\chi^2_{\rm reduced}$ for the CIGALE fits to the LVL sample is 0.81 with a 1σ dispersion of 0.41, reflecting that the SED fits are generally reasonable for the sample. Moreover, given that most $\chi^2_{\rm reduced}$ values are less

than unity, the distribution suggests that the typical photometric uncertainties are overestimated. However, our $\chi^2_{\rm reduced}$ are driven to artificially lower values since we incorporate a 10% across-the-board increase in our flux uncertainties (additionalerror = 0.1) in our SED fitting. If we instead reduce the additional flux uncertainty to 5%, the median $\chi^2_{\rm reduced}$ increases to 1.54 and the scatter grows to 0.77. 94% of the SED fits yield $\chi^2_{\rm reduced} < 3$ and all but four fits (>98%) result in $\chi^2_{\rm reduced} < 4$. The galaxies with $\chi^2_{\rm reduced} > 3$ are generally low-mass galaxies ($\log_{10} M_*/M_\odot \lesssim 8$) with suspect photometry. Though there is a large fraction of galaxies (51%) with a best-fit stellar metallicity of $Z = 0.004$ ($1/5{\rm th} Z_\odot$ like the SMC), these are nearly all dwarf galaxy systems with $M_* < 10^9 M_\odot$ and thus are expected to have significantly subsolar metal abundances (Lee et al. 2006; Kirby et al. 2013). The remaining systems have best-fit metallicities of $0.4 Z_\odot$ (27%), $Z_\odot$ (16%), and $Z = 2.5 Z_\odot$ (5%). We note that there is no trend in $\chi^2_{\rm reduced} > 3$ with the number of SED data points used in the fit.

Figure 4 provides the distributions of Bayesian-based values for several main parameters in the CIGALE fits. We include in Figure 4 comparisons with results from other surveys. The magenta histogram for $A_{\rm H\alpha}$ attenuations derives from the Lee et al. (2009b) 11HUGS survey of ~300 star-forming galaxies, and the red histograms for γ, $q_{\rm PAH}$, and $U_{\rm min}$ come from the Draine et al. (2007) analysis of 75 nearby star-forming galaxies from SINGS (Kennicutt et al. 2003). The median values and the 25th–75th percentile ranges for these key parameters are provided in Table 3. The distribution of LVL $A_{\rm H\alpha}$ values displayed in Figure 4 is qualitatively similar to the distribution of values for the 11HUGS sample, and the sample medians are quite close: 0.16 mag for LVL and 0.18 mag for 11HUGS. An additional comparison point is that from the sample of ~700,000 $z < 0.3$ galaxies of Salim et al. (2016; see also Salim & Narayanan 2020), which also has a median $A_{\rm H\alpha}$ value of 0.16 mag (where we have assumed $A_{\rm H\alpha} = 0.783 A_V$ from the Draine 2003 reddening curve).

Two additional parameters that are allowed to vary are alpha and E_BV_factor (see Table 2). The majority (56.2%) of the best-fit solutions for the radiation field power-law exponent alpha is 2.0, matching the fixed value adopted by Draine et al. (2007) who find their fits to nearby galaxy SEDs are largely insensitive to the particular choice for alpha. Also consistent with previous efforts are the fit results for E_BV_factor: 81% of our best-fit values for E_BV_factor are either 0.25 or 0.50, values which bracket the recommended value of 0.44 recommended by Calzetti et al. (2000).

The panels in Figure 4 presenting the CIGALE-based fit distributions for the dust parameters $q_{\rm PAH}$, γ, and $U_{\rm min}$ are in reasonable agreement with published distributions for normal star-forming galaxies; the (non-CIGALE-based) fit values for these three parameters from the analysis of SINGS galaxies (Kennicutt et al. 2003) are similar to what we find for the LVL sample with CIGALE fits (Draine et al. 2007; Dale et al. 2012). One clear discrepancy, however, is that the LVL distribution for γ is shifted to larger values than what Draine et al. (2007) find for the SINGS sample. The dust parameter γ is an indicator of the fraction of the interstellar dust that is heated by intense starlight such as in photodissociation regions that are associated with star-forming regions, i.e., not the bulk of the dust that is more gently heated throughout the diffuse interstellar medium
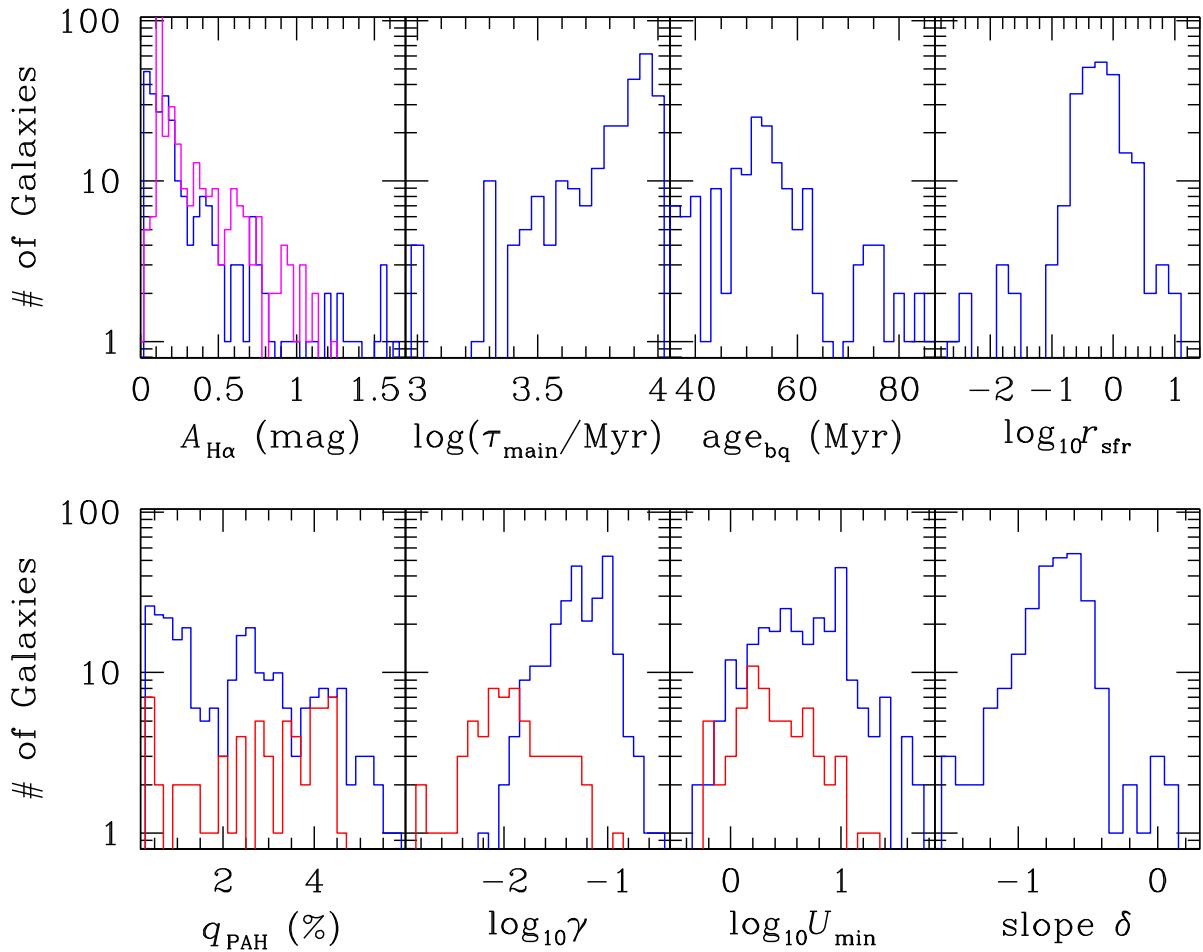
Figure 4. The distributions of Bayesian-based fit values for several key parameters are plotted in blue. The red histograms overlaid for the dust parameters γ, q_{PAH}, and U_{min} show the values from the spectral analysis of the SINGS sample of nearby galaxies in Draine et al. (2007). The magenta histogram for $A_{H\alpha}$ shows the distribution for the 11HUGS survey that has large overlap with LVL (Lee et al. 2009b). Table 3 provides the median values and the 25th–75th percentile ranges for these parameters.

Table 3
SED Fit Medians and 25th–75th Percentile Ranges

Parameter	Median	25th–75th Percentile Range
$\chi^2_{reduced}$	0.81	0.41
$A_{H\alpha}$ (mag)	0.16	0.14
Slope modifier δ	−0.71	0.13
$\log_{10}(\tau_{main}/Myr)$	3.90	0.11
r_{sfr}	0.52	0.33
$\log_{10}\gamma$	−1.26	0.19
q_{PAH} (%)	2.16	1.15
$\log_{10} U_{min}$	0.68	0.31
age_{bq} (Myr)	47.	15.

of a galaxy. This discrepancy is likely due to the LVL sample having a larger fraction of bursty star-forming dwarf galaxies, e.g., 58 LVL galaxies have SED fits with r_{SFR} values greater than unity (see Figure 4).

We caution that any detailed comparisons between the results from our work and those from other efforts is limited by the different approaches to the SED fitting as well as the samples and data involved. For example, the $A_{H\alpha}$ attenuations from Lee et al. (2009b) are ultimately derived from a measured Balmer decrement. In addition, Draine et al. (2007) do not use

an SED fitting procedure that balances the energy absorbed by dust at shorter wavelengths with the dust emission observed at longer wavelengths. Also, CIGALE adopts $U_{max} = 10^7$ for the maximum value of the radiation field that heats the dust in units of the local interstellar radiation field (Dale et al. 2001) whereas only ∼8% of the fit values drawn from Draine et al. (2007) employ the same maximum U (the remainder of the Draine et al. 2007 fit values portrayed in Figure 4 are based on $U_{max} = 10^6$). Finally, Janowiecki et al. (2017) study extreme starbursting blue compact dwarf galaxies and they adopt an exponentially-decaying star-formation history for their CIGALE SED fits while we assume a (similar but) delayed exponential star-formation history.

Another approach to assessing the robustness of the SED fits is to compare the fit parameters to those obtained when mock SEDs are fit, since the physical properties of the mock systems are precisely known. CIGALE has built-in functionality for executing mock SED fits; for a given object the fluxes for the best-fit model are modified by adding values drawn from Gaussian distributions with 1σ values that match the flux uncertainties. Based on the level of agreement between the mock fit parameter values and our best-fit parameter values, the inference is that for our work there are three parameters that are less well constrained than the remaining parameters: γ, δ, and α. For all three of these parameters, a comparison of the mock
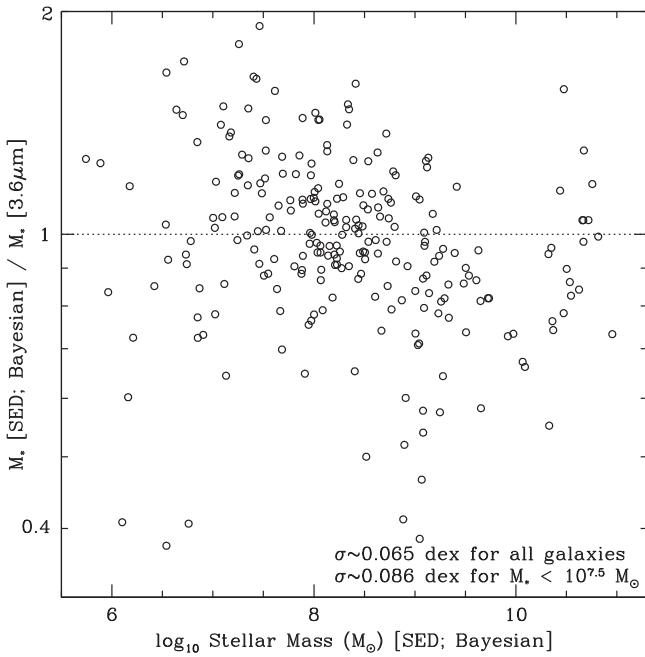
Figure 5. Comparison of CIGALE SED-based stellar masses with those derived from 3.6 μm infrared photometry. The 3.6 μm—based stellar masses are computed using a mass-to-light ratio that depends on the specific star-formation rate following Appendix A.4 of Leroy et al. (2019). The horizontal dotted line indicates unity for the mass ratio.

and best-fit parameters values yields a Spearman's rank correlation coefficient less than 0.7 and an r^2 value for a linear regression less than 0.15. This result is similar to those from other CIGALE-based galaxy SED fitting studies where the shapes of the dust SED (α) and the assumed attenuation curve (δ) are the least reliable fit parameters (e.g., Giovannoli et al. 2011; Boquien et al. 2012).

Figure 5 provides a comparison of the (Bayesian) SED-based stellar masses with those from single-band photometry assuming a mass-to-light ratio that depends on the specific star-formation rate following Appendix A.4 of Leroy et al. (2019; see also McGaugh & Schombert 2014; Meidt et al. 2014; Hunt et al. 2019). There is general agreement between the stellar mass measures; the median ratio of the 3.6 μm-based-to-SED-based stellar masses agree within 0.01 dex of unity, and the dispersion (i.e., random scatter) is 0.065 dex. There is a weak trend in Figure 5 as a function of the single-band-based stellar mass (Spearman's rank correlation coefficient of -0.29), and the scatter is somewhat enhanced for the lower-mass systems; the scatter for galaxies with $\log_{10} M_*/M_\odot < 7.5$—galaxies for which the photometry is more challenging given their fainter flux levels—is 0.086 dex.

The left panel of Figure 6 shows the trend in dust-to-stellar mass as a function of stellar mass, and the right panel shows the same ratio as a function of the star-formation rate averaged over the past 100 Myr. The median logarithmic ratio in M_{dust}/M_* for all LVL galaxies with secure dust masses is -3.2 with a dispersion of 0.36 dex. The fit values from the Hunt et al. (2019) CIGALE analysis of the KINGFISH sample of 61 nearby galaxies (Kennicutt et al. 2011) are included as open red triangles; clearly the KINGFISH sample is skewed, on average, to larger stellar masses and larger star-formation rates compared to LVL. We also provide data from the Rémy-Ruyer et al. (2015; see also Hunt et al. 2019) analysis of the DGS; the DGS data are more scattered. There are positive correlations in Figure 6 for the LVL sample, with Spearman's rank correlation coefficient values ρ of 0.58 and 0.65, respectively, for the left-hand and right-hand panels. The trend seen in the right-hand panel for the LVL sample echoes that seen for the more actively star-forming KINGFISH sample ($\log_{10} SFR_{100}(M_\odot \mathrm{yr}^{-1}) > -3$; Spearman's rank correlation coefficient $\rho = 0.40$).
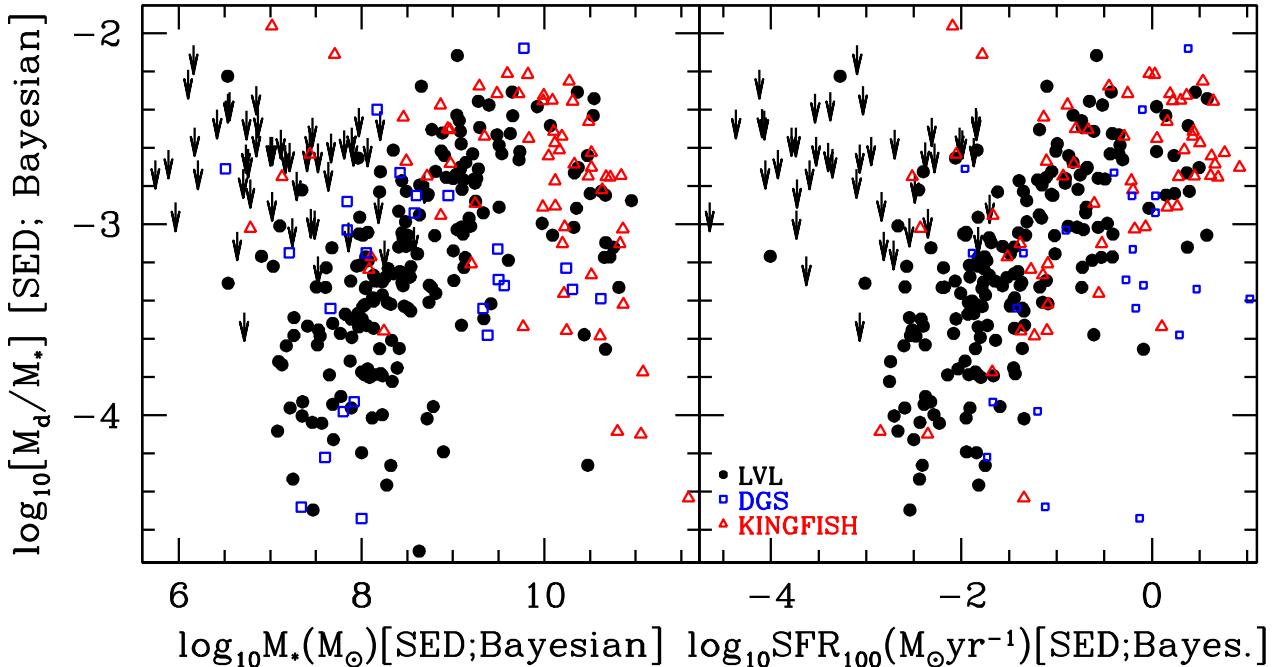
Figure 6. Left: dust-to-stellar mass as a function of stellar mass. Filled circles indicate our results for the LVL sample, the open red triangles are from the CIGALE SED fits for the KINGFISH sample from Hunt et al. (2019), and the open blue squares represent the SED-based values from the Dwarf Galaxy Sample presented in Rémy-Ruyer et al. (2015). Right: dust-to-stellar mass as a function of star-formation rate averaged over the past 100 Myr, as inferred from the SED fitting (the star-formation rates for the DGS sample are based on Hα+TIR).
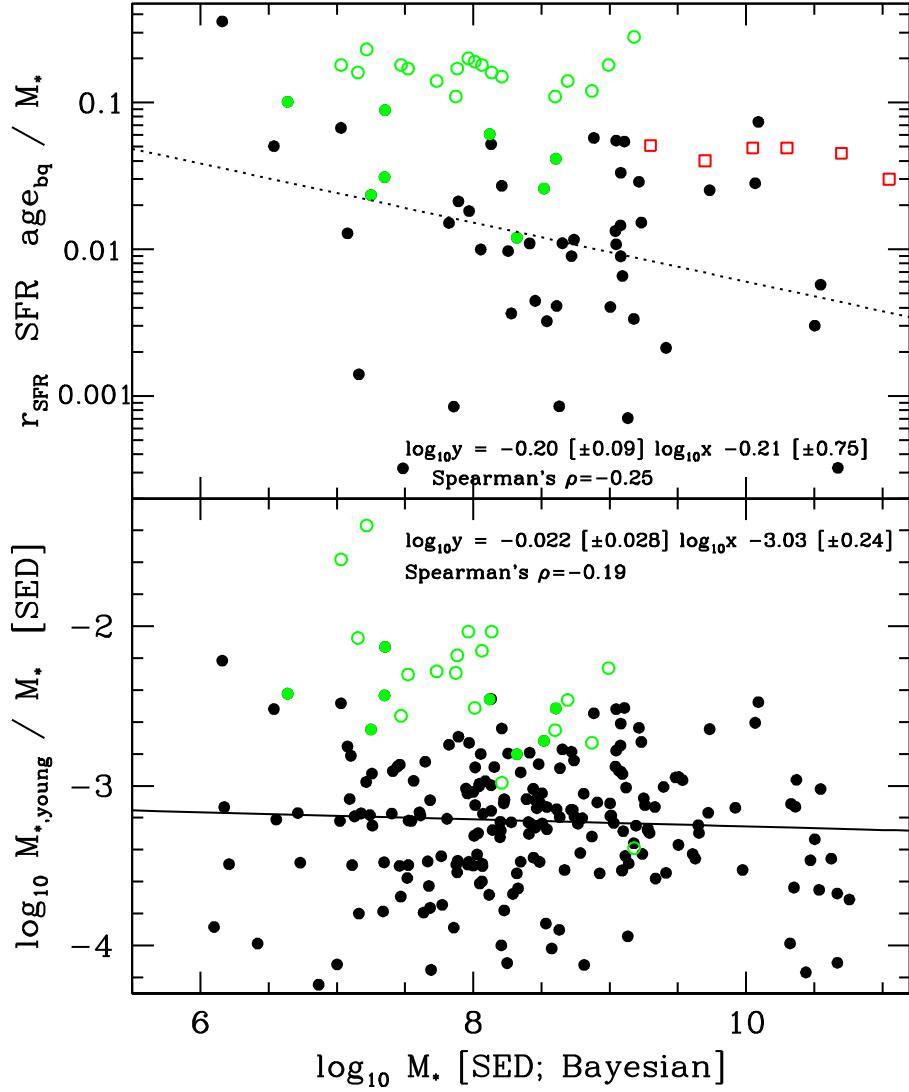
Figure 7. Top: the fraction of stellar mass in the modeled late burst of star formation compared to the total stellar mass in the galaxy, as a function of total stellar mass. Bottom: the ratio of the mass in the young stellar population (<10 Myr) to the total mass of the stellar population. Filled circles correspond to LVL galaxies; those in green indicate blue compact dwarf galaxies in the LVL sample. The green open circles are from the Janowiecki et al. (2017) survey of blue compact dwarf galaxies and the red open squares are from the Bergvall et al. (2016) study of SDSS starbursting galaxies. Note that the upper panel is restricted to late bursts and not late quenching episodes (i.e., $r_{\rm SFR} > 1$).

The top panel of Figure 7 shows how the modeled fraction of stellar mass that derives from the late burst of star formation varies with total stellar mass, and the bottom panel displays the modeled ratio of stellar mass currently appearing in young stars (<10 Myr) to the total stellar mass, again as a function of the total stellar mass. Both panels in Figure 7 show a modest decreasing trend with total stellar mass. The burst fraction (top panel) is larger than the current young stellar mass fraction (bottom panel) due to young massive stars dying more quickly than older stars. We note that a typical LVL galaxy has $\log_{10} M_{*,<10\,{\rm Myr}}/M_* \sim -3$, which roughly corresponds to the current star formation being the same as its average past value over the age of the disk. To promote a fair comparison with the work of Janowiecki et al. (2017), we have restricted the upper panel to only LVL galaxies where the late episode is a burst ($r_{\rm SFR} > 1$) and not a quenching event ($r_{\rm SFR} < 1$). Nonetheless, the comparison with Janowiecki et al. (2017) still is not perfect, as their delayed star-formation history adopts an exponentially-decaying late burst whereas our delayed star-formation history

uses a constant late star-formation rate that lasts for age_bq (see Equation (1)). The values from the Janowiecki et al. (2017) study lie at relatively higher values of burst fractions and higher values of young-to-total stellar mass ratios, not surprising given the nature of their sample of starbursting blue compact dwarf galaxies. It is interesting to note that the eight LVL galaxies that have been classified as blue compact dwarfs (Gil de Paz et al. 2003; Kennicutt et al. 2008; Lee et al. 2009a) also appear at elevated values in both panels of Figure 7. Another useful comparison sample provided in the top panel of Figure 7 is that of Bergvall et al. (2016). They define starburst galaxies as having a birthrate parameter $b = {\rm SFR}/\langle {\rm SFR}\rangle \geqslant 3$, and find that 1% of star-forming galaxies SDSS DR7 galaxies qualify as starbursting. Over their starburst subsample's stellar mass range of $\log_{10} M_*/M_\odot \sim 9$–11.5, they find higher burst fractions than we do for the LVL sample over a broader stellar mass range ($\log_{10} M_*/M_\odot \sim 6$–11): their median trend is within ~0.02–0.05 whereas we find a fitted trend with amplitude ~0.004–0.04. Interestingly, the strongest decreasing trend with
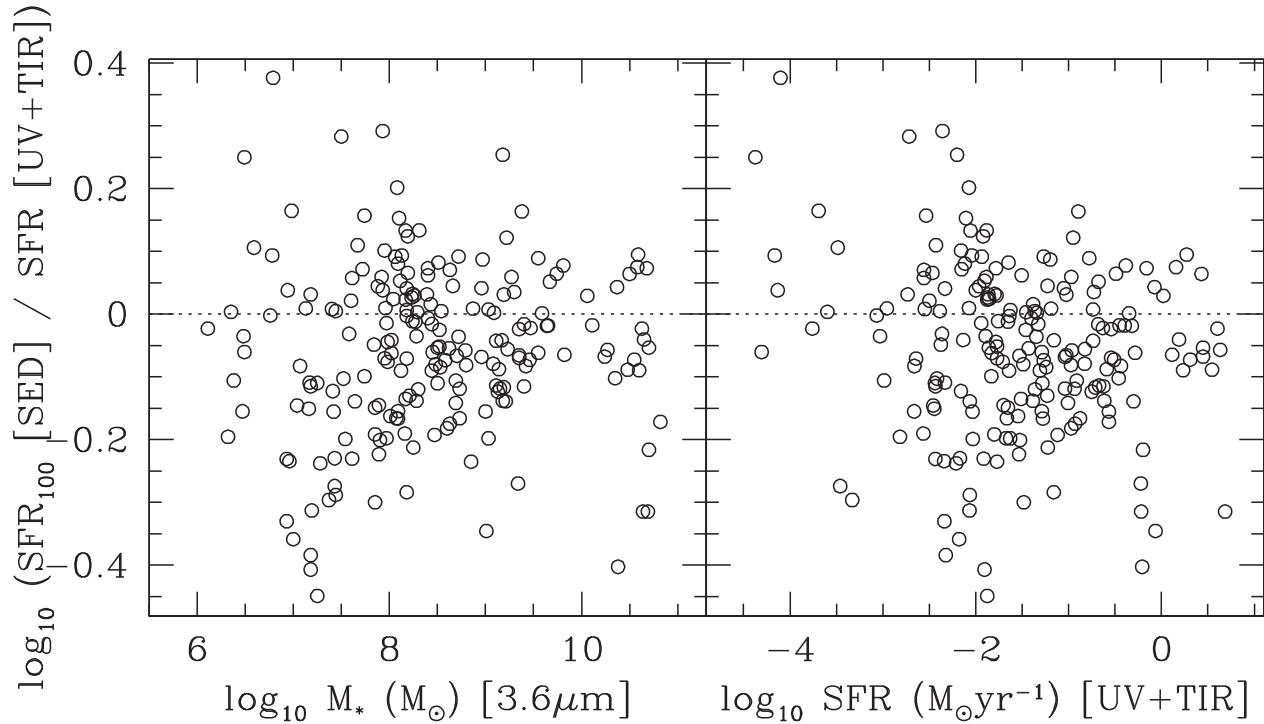
Figure 8. The (Bayesian-based) star-formation rate from the SED fit averaged over 100 Myr compared to the star-formation rate derived from hybrid indicators of ultraviolet + total infrared (Hao et al. 2011). The left-hand panel is plotted as a function of the 3.6 μm—based stellar mass and the right-hand panel is shown as a function of hybrid-based star-formation rates. The horizontal dotted line indicates unity or perfect agreement between the star-formation rates.
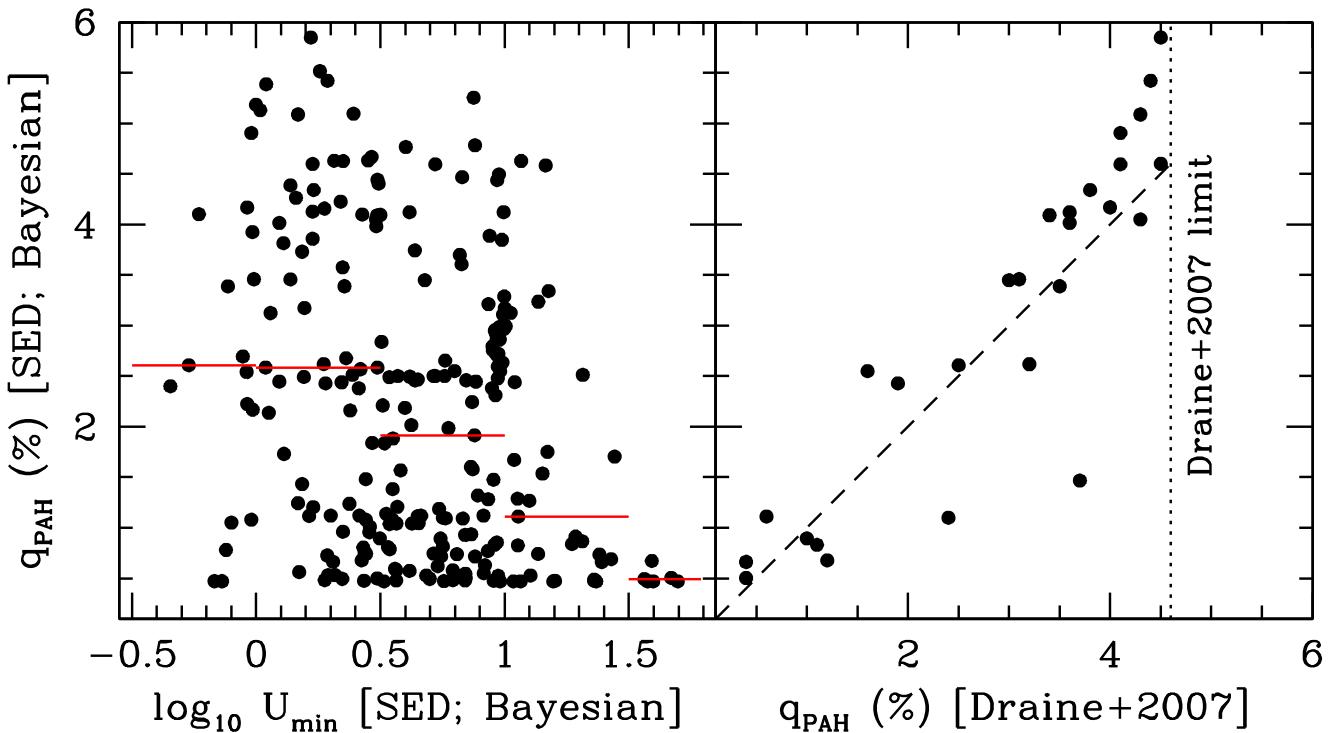
Figure 9. The fractional mass abundance of PAHS vs. minimum interstellar radiation field intensity (left) and the fractional PAH mass abundance from the SED fitting work of Draine et al. (2007) for the subset of the LVL sample that overlaps with the SINGS sample (right). The median values for several bins are provided in the left-hand panel, the dotted line in the right-hand panel indicates the maximum possible value for the Draine et al. (2007) SED fits, and the dashed line in the right-hand panel indicates the 1-to-1 relation.

mass found in Bergvall et al. (2016) is for poststarburst galaxies.

Figure 8 displays how the star-formation rate estimates compare between those derived on 100 Myr timescales from the SED fitting and those derived from the "empirical" ultraviolet + total infrared measurements (which also trace the star-formation rate on 100 Myr timescales; Hao et al. 2011; Kennicutt & Evans 2012). There is no dependence on the ratio

Table 4
Spatially-integrated Photometry Corrected for Neither Galactic Nor Intrinsic Extinction

Filter	GALEX FUV	GALEX NUV	U	B	V	R_C	SDSS u	SDSS g	SDSS r
$\overline{\lambda}(\mu m)$	0.154	0.231	0.361	0.443	0.551	0.659	0.356	0.482	0.626
$\Delta\lambda(\mu m)$	0.025	0.073	0.064	0.099	0.089	0.159	0.056	0.127	0.133
A_λ/A_V	2.586	2.994	1.556	1.291	1.0	0.795	1.589	1.206	0.854
WLM	280 ± 044E−2	313 ± 047E−2	⋯	100 ± 002E−1	145 ± 004E−1	173 ± 004E−1	⋯	⋯	⋯
NGC0024	772 ± 121E−3	981 ± 149E−3	⋯	496 ± 013E−2	879 ± 024E−2	972 ± 026E−2	⋯	⋯	⋯
NGC0045	291 ± 045E−2	356 ± 055E−2	642 ± 017E−2	128 ± 003E−1	199 ± 005E−1	226 ± 006E−1	⋯	⋯	⋯
NGC0055	277 ± 043E−1	356 ± 055E−1	⋯	⋯	⋯	⋯	⋯	⋯	⋯
NGC0059	⋯	⋯	928 ± 025E−3	212 ± 005E−2	380 ± 010E−2	492 ± 013E−2	⋯	⋯	⋯

Notes. The compact table entry format TUV ± WXYEZ implies (T.UV ± W.XY)×10^Z in Jy for the broadband filters and 10^{-15} W m^{-2} for Hα. Corrections for neither Galactic nor intrinsic extinction have been applied (see Section 3). 5σ upper limits are provided for non-detections. No color corrections have been applied. The filter central wavelengths and widths are computed via Equations (1) and (2) of Dale et al. (2017).
[a] The Spitzer MIPS data for NGC 3034 suffer from saturation and thus the tabulated values are lower limits.

Table 4 is published in its entirety in the electronic edition of the Astronomical Journal. A portion is shown here for guidance regarding its form and content. The full version has many more columns of flux densities in different bands.
(This table is available in its entirety in machine-readable form.)

of modeled-to-empirical star-formation rate indicators as a function of either stellar mass or star-formation rate, and the median of the distribution is −0.055 dex with a scatter of 0.13 dex. In other words, the modeled star-formation rates for the bulk of the sample are about 88% of the empirical values, on average. The scatter is driven by outliers with ordinate (y-axis) values more than ∼0.2 dex from perfect agreement ($|\log 10(\mathrm{SFR}_{100}[\mathrm{SED}]/\mathrm{SFR}[\mathrm{UV}+\mathrm{TIR}]| > 0.2$). Inspection of the CIGALE fits shows that a large number of these outliers have only upper limits for the MIPS infrared fluxes (and thus their UV + TIR star-formation rates are compromised). For reference, Salim et al. (2016) find good one-to-one agreement and a scatter of 0.2 dex when comparing their CIGALE-based star-formation rates with those from SDSS spectroscopy. As a reminder, our sample is dominated by dwarf galaxies, which we define here as $\log_{10} M_*/M_\odot < 9$; fully 75% of LVL galaxies satisfy this dwarf status criterion. In contrast, the SDSS-based work of Salim et al. (2016) has only 1.5% of their sample below this dwarf galaxy stellar mass threshold. The LVL sample is also dominated by low-metallicity systems, which helps to explain the (small) discrepancy noted above between the SED-based and the UV + TIR-based values. As noted by Kennicutt & Evans (2012), lower metallicity systems have enhanced ultraviolet emissivity for a given star-formation rate (∼0.07 dex for $Z = 0.1Z_\odot$).

A final analysis of the SED fits is provided in Figure 9, which displays the fractional mass abundance of PAHs as a function of minimum interstellar radiation field that heats the dust in the diffuse ISM, as inferred from the SED fits, and the fractional PAH mass abundance for the subset of LVL galaxies that are in the SINGS sample and were fit by Draine et al. (2007). Previous studies of PAH abundances have shown that the strength of PAH emission is sensitive to the hardness of the interstellar radiation field, the metal abundance, molecular gas surface density, star-formation activity level (star-formation rate, dust temperature, etc.), or some combination thereof (e.g., Engelbracht et al. 2005; Madden et al. 2006; Wu et al. 2006; Draine et al. 2007; Engelbracht et al. 2008; Dale et al. 2009; Sandstrom et al. 2010; Wu et al. 2010; Rémy-Ruyer et al. 2015; Chastenet et al. 2019; Galliano et al. 2021; Dale et al. 2023). The LVL sample is a useful testbed for examining how dwarf galaxies and their generally lower metallicities and harder radiation fields affect PAHs. The left-hand panel of Figure 9 shows that q_{PAH} decreases as a function of the intensity of radiation field that heats the diffuse interstellar medium, suggesting that the radiation field plays a role in processing (e.g., ionizing, destroying) small dust grains/molecules. The right-hand panel of Figure 9 indicates that our SED fits provide fractional PAH mass abundances that are consistent with other independent SED-fitting efforts.

6. Summary

We have carried out a detailed study of the spectral energy distributions for the 258 galaxies in the Local Volume Legacy program. This volume-limited sample presents a statistically representative view of the overall galaxy population in the local universe; approximately three quarters of the sample is classified as dwarf galaxies with $\log_{10} M_*/M_\odot < 9$, a portion of parameter space that is rarely studied with statistically large samples of star-forming galaxies. The data set utilized here involves fluxes at 26 different wavelengths spanning the far-ultraviolet through the far-infrared. The CIGALE fitting code was used to characterize each galaxy's physical properties assuming a delayed star-formation history along with a late starburst/quenching episode. Reasonable fits ($\chi^2_{\mathrm{reduced}} < 3$) are obtained for 94% of the sample, and the SED-derived stellar masses agree with those traditionally derived from near-infrared photometry to within better than 0.1 dex. We find that the stellar mass fraction arising from the modeled late bursts decreases for increasingly massive galaxies, consistent with the notion that low-mass dwarf galaxies are more likely to experience bursty star-formation histories than massive star-forming galaxies (e.g., Weisz et al. 2012). We also find that the SED-derived star-formation rates for LVL galaxies are on average 88% the values obtained from "empirical" hybrid star-formation rate indicators. Finally, the SED fits indicate that the PAH fractional dust mass decreases for increasing values of the radiation field that heats the dust dispersed throughout the diffuse interstellar medium.

Table 5
SED-fit Values

Name	$\chi^2_{\rm red}$	$A_{\rm H\alpha}$ (mag)	δ	$\log_{10} \tau_{\rm main}$ (Myr)	$\log_{10} r_{\rm SFR}$	$\log_{10} \gamma$	$q_{\rm PAH}$ (%)	$\log_{10} U_{\rm min}$	SFR$_{100}$ ($M_\odot {\rm yr}^{-1}$)	$\log_{10} M_{\rm dust}$ ($M_\odot$)	$\log_{10} M_*$ ($M_\odot$)
WLM	2.37	0.07 ± 0.03	−0.6 ± 0.5	3.97 ± 0.05	0.35 ± 0.10	−0.99 ± 0.56	1.57 ± 0.70	0.58 ± 0.29	−2.55 ± 0.03	3.77 ± 0.28	7.26 ± 0.02
NGC0024	0.37	0.40 ± 0.15	−0.5 ± 0.4	3.73 ± 0.15	0.44 ± 0.16	−0.96 ± 0.49	3.46 ± 0.72	0.14 ± 0.27	−0.91 ± 0.10	6.46 ± 0.25	9.24 ± 0.05
NGC0045	2.28	0.18 ± 0.06	−0.9 ± 0.4	3.97 ± 0.05	0.78 ± 0.13	−0.89 ± 0.46	2.58 ± 0.35	0.04 ± 0.30	−0.74 ± 0.03	6.61 ± 0.25	9.07 ± 0.02
NGC0055	1.10	0.38 ± 0.15	−0.6 ± 0.5	3.88 ± 0.14	2.29 ± 1.05	−1.05 ± 0.61	1.12 ± 0.02	0.42 ± 0.21	−0.61 ± 0.09	6.57 ± 0.21	9.08 ± 0.07
NGC0059	0.30	0.17 ± 0.06	−0.7 ± 0.5	3.32 ± 0.06	1.22 ± 0.36	−1.06 ± 0.57	0.66 ± 0.30	1.39 ± 0.21	−2.27 ± 0.11	3.92 ± 0.24	8.63 ± 0.04
ESO410-G005	1.32	0.15 ± 0.11	−0.8 ± 0.5	3.93 ± 0.09	0.00 ± 0.03	−1.27 ± 0.71	4.44 ± 1.85	0.97 ± 0.71	−3.35 ± 0.12	<4.15	6.76 ± 0.05
Sculptor-dE1	1.39	0.29 ± 0.51	−0.8 ± 0.5	3.29 ± 0.53	1.25 ± 1.62	−1.26 ± 0.71	2.99 ± 2.17	1.00 ± 0.68	−4.46 ± 1.23	<4.60	6.91 ± 0.10
ESO294-G010	1.11	0.08 ± 0.08	−0.8 ± 0.5	3.61 ± 0.18	0.14 ± 0.27	−1.32 ± 0.76	2.72 ± 2.11	0.97 ± 0.70	−3.73 ± 0.19	<4.02	6.78 ± 0.08
IC1574	2.39	0.04 ± 0.03	−0.6 ± 0.5	3.66 ± 0.08	0.20 ± 0.02	−1.38 ± 0.81	1.48 ± 1.33	0.96 ± 0.72	−2.48 ± 0.06	<4.96	7.64 ± 0.04
NGC0247	3.38	0.20 ± 0.08	−0.9 ± 0.5	3.91 ± 0.09	0.37 ± 0.10	−1.97 ± 1.52	0.47 ± 0.03	−0.17 ± 0.24	−0.65 ± 0.09	6.92 ± 0.30	9.28 ± 0.04
NGC0253	0.59	1.29 ± 0.30	0.1 ± 0.1	3.60 ± 0.14	0.41 ± 0.52	−1.50 ± 0.11	2.46 ± 0.24	0.85 ± 0.25	0.37 ± 0.15	7.64 ± 0.20	10.76 ± 0.07
ESO540-G030	0.50	0.15 ± 0.16	−0.8 ± 0.5	3.82 ± 0.15	0.02 ± 0.07	−1.28 ± 0.72	2.99 ± 2.15	0.99 ± 0.68	−3.74 ± 0.41	<4.35	6.85 ± 0.07
UGCA015	3.78	0.14 ± 0.09	−0.6 ± 0.4	4.00 ± 0.01	0.00 ± 0.00	−1.32 ± 0.75	3.89 ± 1.77	0.94 ± 0.74	−3.03 ± 0.02	<4.57	6.84 ± 0.02
ESO540-G032	1.00	0.15 ± 0.15	−0.9 ± 0.5	3.63 ± 0.18	0.09 ± 0.24	−1.32 ± 0.76	2.55 ± 2.08	0.98 ± 0.69	−4.07 ± 0.43	<4.33	6.74 ± 0.09
UGC00521	0.44	0.04 ± 0.02	−0.5 ± 0.5	3.82 ± 0.15	1.88 ± 1.06	−1.16 ± 0.63	0.69 ± 0.31	1.43 ± 0.33	−1.85 ± 0.07	<5.58	7.97 ± 0.07
SMC	0.70	0.17 ± 0.06	−0.6 ± 0.5	3.68 ± 0.21	1.09 ± 1.08	−1.19 ± 0.61	0.48 ± 0.08	0.56 ± 0.30	−1.65 ± 0.14	5.32 ± 0.33	8.54 ± 0.09
NGC0300	1.43	0.36 ± 0.10	−0.4 ± 0.4	3.83 ± 0.16	1.63 ± 1.75	−1.04 ± 0.53	2.14 ± 0.61	0.05 ± 0.28	−0.83 ± 0.06	6.61 ± 0.36	9.04 ± 0.08
UGC00668	3.10	0.04 ± 0.02	−0.9 ± 0.5	3.97 ± 0.06	0.98 ± 0.20	−0.83 ± 0.36	0.56 ± 0.23	0.17 ± 0.30	−2.67 ± 0.03	4.09 ± 0.26	7.10 ± 0.02
UGC00685	1.24	0.10 ± 0.05	−0.8 ± 0.5	3.66 ± 0.15	0.51 ± 0.21	−1.39 ± 0.96	0.96 ± 0.31	0.46 ± 0.28	−2.42 ± 0.10	4.39 ± 0.24	7.89 ± 0.06
UGC00695	0.66	0.15 ± 0.06	−0.8 ± 0.5	3.92 ± 0.08	0.35 ± 0.09	−2.23 ± 1.03	0.53 ± 0.18	0.68 ± 0.17	−1.84 ± 0.06	4.61 ± 0.18	8.04 ± 0.04
NGC0404	0.52	0.51 ± 0.24	−1.3 ± 0.2	3.79 ± 0.18	0.03 ± 0.11	−0.88 ± 0.43	1.91 ± 0.97	0.88 ± 0.24	−1.95 ± 0.47	4.70 ± 0.16	8.90 ± 0.08
UGC00891	3.93	0.09 ± 0.04	−0.7 ± 0.5	3.77 ± 0.13	0.20 ± 0.02	−1.42 ± 0.93	1.24 ± 0.70	0.38 ± 0.70	−1.77 ± 0.07	5.06 ± 0.47	8.29 ± 0.06
UGC01056	2.74	0.08 ± 0.04	−0.9 ± 0.5	3.91 ± 0.10	0.81 ± 0.18	−1.32 ± 0.75	1.67 ± 0.81	1.04 ± 0.36	−1.80 ± 0.04	4.29 ± 0.26	8.09 ± 0.05
UGC01104	0.39	0.07 ± 0.03	−0.6 ± 0.5	3.93 ± 0.09	0.26 ± 0.09	−1.40 ± 0.76	2.44 ± 0.59	0.88 ± 0.29	−1.83 ± 0.05	4.24 ± 0.23	8.03 ± 0.04
NGC0598	0.96	0.60 ± 0.20	−0.6 ± 0.5	3.88 ± 0.15	3.07 ± 1.83	−1.14 ± 0.62	4.13 ± 0.54	0.23 ± 0.26	−0.58 ± 0.11	6.93 ± 0.25	9.05 ± 0.07
NGC0625	0.39	0.30 ± 0.12	−1.1 ± 0.4	3.70 ± 0.17	0.88 ± 0.40	−1.33 ± 0.11	0.62 ± 0.27	0.73 ± 0.25	−1.38 ± 0.06	5.42 ± 0.19	8.74 ± 0.06
NGC0628	0.61	0.75 ± 0.15	−0.7 ± 0.3	3.93 ± 0.08	0.50 ± 0.13	−1.35 ± 0.88	5.09 ± 0.94	0.17 ± 0.26	0.05 ± 0.06	7.54 ± 0.24	9.92 ± 0.04
UGC01176	1.46	0.10 ± 0.04	−0.6 ± 0.5	3.96 ± 0.06	0.39 ± 0.05	−1.83 ± 0.55	1.08 ± 0.49	−0.02 ± 0.46	−1.62 ± 0.02	5.37 ± 0.39	8.20 ± 0.03
ESO245-G005	1.32	0.07 ± 0.03	−0.6 ± 0.5	3.98 ± 0.06	0.64 ± 0.09	−1.52 ± 1.12	0.49 ± 0.12	0.35 ± 0.16	−1.76 ± 0.04	4.87 ± 0.23	8.04 ± 0.02
UGC01249	0.92	0.20 ± 0.06	−0.5 ± 0.5	3.96 ± 0.06	0.41 ± 0.05	−1.05 ± 0.61	0.74 ± 0.32	0.44 ± 0.21	−1.02 ± 0.04	5.74 ± 0.21	8.80 ± 0.03
NGC0672	0.75	0.29 ± 0.11	−1.0 ± 0.4	3.89 ± 0.10	0.40 ± 0.10	−2.00 ± 0.38	1.12 ± 0.05	0.21 ± 0.22	−0.69 ± 0.09	6.57 ± 0.21	9.28 ± 0.04
ESO245-G007	1.27	0.04 ± 0.03	−0.7 ± 0.5	3.84 ± 0.15	0.03 ± 0.13	−1.35 ± 0.79	2.31 ± 1.98	0.96 ± 0.71	−4.64 ± 0.37	⋯	5.96 ± 0.07
NGC0784	1.08	0.08 ± 0.04	−0.8 ± 0.5	3.92 ± 0.10	0.52 ± 0.14	−1.13 ± 0.69	0.58 ± 0.24	0.56 ± 0.21	−1.49 ± 0.08	5.04 ± 0.19	8.47 ± 0.04
NGC0855	0.44	0.42 ± 0.16	−1.2 ± 0.2	3.50 ± 0.07	0.76 ± 0.32	−1.00 ± 0.56	2.55 ± 0.27	0.80 ± 0.20	−1.34 ± 0.06	5.56 ± 0.16	9.09 ± 0.04
ESO115-G021	0.42	0.08 ± 0.03	−0.7 ± 0.5	3.81 ± 0.15	0.67 ± 0.23	−0.99 ± 0.54	0.74 ± 0.32	0.44 ± 0.27	−1.89 ± 0.07	4.73 ± 0.23	8.13 ± 0.06
ESO154-G023	1.43	0.12 ± 0.05	−0.6 ± 0.5	3.92 ± 0.09	0.54 ± 0.15	−1.00 ± 0.57	0.59 ± 0.25	0.56 ± 0.25	−1.34 ± 0.07	5.08 ± 0.23	8.54 ± 0.04
NGC1291	0.62	0.27 ± 0.16	−0.7 ± 0.5	3.28 ± 0.06	0.82 ± 2.62	−1.48 ± 1.01	2.61 ± 1.20	−0.27 ± 0.20	−0.74 ± 0.33	7.49 ± 0.28	10.82 ± 0.04
NGC1313	2.21	0.49 ± 0.07	−0.6 ± 0.4	3.96 ± 0.07	1.23 ± 0.23	−1.05 ± 0.63	2.47 ± 0.21	0.65 ± 0.22	−0.49 ± 0.04	6.47 ± 0.20	9.23 ± 0.03
NGC1311	0.36	0.13 ± 0.05	−0.9 ± 0.5	3.85 ± 0.12	0.65 ± 0.17	−0.98 ± 0.52	1.08 ± 0.15	0.55 ± 0.21	−1.77 ± 0.07	4.92 ± 0.20	8.22 ± 0.05
UGC02716	1.13	0.10 ± 0.04	−1.0 ± 0.4	3.75 ± 0.10	0.20 ± 0.00	−1.05 ± 0.56	4.12 ± 0.99	1.00 ± 0.38	−1.95 ± 0.06	4.10 ± 0.23	8.12 ± 0.04
IC1959	1.15	0.16 ± 0.05	−0.8 ± 0.5	3.97 ± 0.06	0.83 ± 0.13	−0.95 ± 0.45	1.09 ± 0.13	0.76 ± 0.23	−1.65 ± 0.03	4.86 ± 0.16	8.15 ± 0.03
NGC1487	0.22	0.46 ± 0.11	−0.4 ± 0.4	3.87 ± 0.14	1.03 ± 0.45	−1.37 ± 0.93	2.50 ± 0.09	0.71 ± 0.19	−0.78 ± 0.05	6.08 ± 0.18	9.09 ± 0.06
NGC1510	0.66	0.28 ± 0.10	−0.5 ± 0.4	3.74 ± 0.16	0.82 ± 0.33	−1.33 ± 0.23	0.74 ± 0.32	1.38 ± 0.24	−1.34 ± 0.06	4.70 ± 0.20	8.72 ± 0.06
NGC1512	0.66	0.51 ± 0.22	−0.4 ± 0.4	3.49 ± 0.07	0.90 ± 0.48	−1.03 ± 0.56	4.34 ± 0.81	0.23 ± 0.25	−0.47 ± 0.06	6.98 ± 0.25	9.98 ± 0.05
NGC1522	0.44	0.42 ± 0.11	−0.5 ± 0.4	3.89 ± 0.12	1.25 ± 0.38	−1.49 ± 0.31	0.74 ± 0.32	1.13 ± 0.27	−1.48 ± 0.04	4.90 ± 0.15	8.32 ± 0.05
IC2049	1.46	0.06 ± 0.03	−0.7 ± 0.5	3.76 ± 0.18	1.09 ± 1.02	−1.60 ± 0.87	1.04 ± 0.54	0.54 ± 0.60	−1.57 ± 0.08	5.13 ± 0.45	8.45 ± 0.08
ESO483-G013	0.46	0.17 ± 0.06	−1.0 ± 0.4	3.51 ± 0.07	0.92 ± 0.23	−1.30 ± 0.81	1.11 ± 0.26	1.05 ± 0.22	−1.60 ± 0.04	4.83 ± 0.15	8.78 ± 0.04

Table 5
(Continued)

Name	$\chi^2_{\rm red}$	$A_{\rm H\alpha}$ (mag)	δ	$\log_{10} \tau_{\rm main}$ (Myr)	$\log_{10} r_{\rm SFR}$	$\log_{10} \gamma$	$q_{\rm PAH}$ (%)	$\log_{10} U_{\rm min}$	SFR$_{100}$ ($M_\odot{\rm yr}^{-1}$)	$\log_{10} M_{\rm dust}$ ($M_\odot$)	$\log_{10} M_*$ ($M_\odot$)
ESO158-G003	0.50	0.18 ± 0.08	-0.9 ± 0.5	3.69 ± 0.18	1.11 ± 0.82	-1.22 ± 0.77	2.84 ± 0.61	0.50 ± 0.19	-1.49 ± 0.08	5.46 ± 0.17	8.61 ± 0.07
ESO119-G016	0.91	0.05 ± 0.03	-0.7 ± 0.5	3.85 ± 0.13	0.72 ± 0.20	-1.39 ± 0.88	0.81 ± 0.38	0.53 ± 0.72	-1.75 ± 0.06	4.86 ± 0.52	8.23 ± 0.06
NGC1705	0.55	0.07 ± 0.03	-0.6 ± 0.5	3.92 ± 0.12	2.89 ± 1.39	-1.39 ± 0.75	1.12 ± 0.04	0.91 ± 0.19	-1.44 ± 0.10	4.74 ± 0.17	8.12 ± 0.05
NGC1744	3.10	0.19 ± 0.06	-1.0 ± 0.5	3.99 ± 0.03	0.48 ± 0.10	-1.05 ± 0.60	3.17 ± 0.72	0.19 ± 0.26	-0.87 ± 0.02	6.27 ± 0.23	8.91 ± 0.02
NGC1796	0.19	0.65 ± 0.17	-0.8 ± 0.5	3.80 ± 0.16	1.29 ± 0.65	-1.14 ± 0.66	4.44 ± 0.73	0.49 ± 0.20	-0.83 ± 0.06	6.37 ± 0.18	9.08 ± 0.06
ESO486-G021	0.60	0.20 ± 0.06	-0.5 ± 0.5	3.94 ± 0.08	0.67 ± 0.14	-1.13 ± 0.61	1.19 ± 0.30	0.74 ± 0.21	-1.71 ± 0.05	4.86 ± 0.16	8.13 ± 0.04
NGC1800	0.73	0.22 ± 0.09	-0.8 ± 0.5	3.91 ± 0.10	0.46 ± 0.11	-0.86 ± 0.43	2.46 ± 0.29	0.64 ± 0.21	-1.18 ± 0.08	5.43 ± 0.16	8.76 ± 0.05
UGCA106	1.24	0.20 ± 0.06	-0.5 ± 0.5	3.93 ± 0.09	0.62 ± 0.14	-1.69 ± 1.25	1.24 ± 0.41	0.17 ± 0.24	-1.05 ± 0.06	6.09 ± 0.18	8.81 ± 0.04
LMC	0.37	0.23 ± 0.10	-0.7 ± 0.5	3.83 ± 0.18	3.56 ± 2.26	-1.01 ± 0.53	2.57 ± 0.31	0.42 ± 0.28	-0.78 ± 0.14	6.36 ± 0.27	8.88 ± 0.09
kkh037	0.57	0.14 ± 0.11	-0.8 ± 0.5	3.48 ± 0.02	0.20 ± 0.02	-1.34 ± 0.78	2.80 ± 2.10	0.95 ± 0.72	-3.53 ± 0.10	<4.46	7.00 ± 0.02
NGC2366	0.88	0.12 ± 0.05	-0.8 ± 0.5	3.93 ± 0.10	2.65 ± 1.18	-1.44 ± 0.55	0.49 ± 0.10	1.36 ± 0.28	-1.44 ± 0.10	4.59 ± 0.24	8.13 ± 0.05
UGCA133	26.13	1.50 ± 0.46	-1.4 ± 0.1	3.02 ± 0.21	1.73 ± 2.19	-1.38 ± 0.80	2.71 ± 2.07	0.97 ± 0.71	-5.61 ± 2.77	<4.56	7.29 ± 0.02
NGC2403	0.59	0.40 ± 0.13	-1.1 ± 0.3	3.95 ± 0.07	0.74 ± 0.15	-1.52 ± 1.06	3.39 ± 0.70	0.36 ± 0.20	-0.35 ± 0.04	6.95 ± 0.25	9.48 ± 0.03
NGC2500	0.66	0.37 ± 0.14	-0.4 ± 0.4	3.90 ± 0.11	0.58 ± 0.19	-1.35 ± 0.79	4.10 ± 0.53	0.43 ± 0.19	-0.91 ± 0.07	6.24 ± 0.20	9.00 ± 0.05
NGC2537	0.39	0.39 ± 0.14	-0.7 ± 0.4	3.68 ± 0.15	0.92 ± 0.40	-1.63 ± 0.78	2.65 ± 0.44	0.76 ± 0.18	-1.11 ± 0.06	5.72 ± 0.16	9.01 ± 0.05
UGC04278	0.58	0.19 ± 0.06	-0.6 ± 0.5	3.95 ± 0.07	0.62 ± 0.11	-1.21 ± 0.75	1.14 ± 0.16	0.52 ± 0.19	-1.40 ± 0.05	5.40 ± 0.17	8.44 ± 0.03
UGC04305	1.27	0.08 ± 0.04	-0.8 ± 0.5	3.94 ± 0.08	1.12 ± 0.24	-0.96 ± 0.54	0.50 ± 0.14	0.84 ± 0.21	-1.36 ± 0.03	4.76 ± 0.17	8.41 ± 0.03
NGC2552	0.64	0.18 ± 0.06	-0.9 ± 0.4	3.97 ± 0.05	0.40 ± 0.02	-1.75 ± 1.19	0.96 ± 0.28	0.35 ± 0.19	-1.18 ± 0.03	5.68 ± 0.24	8.63 ± 0.02
M81dwA	2.68	0.47 ± 0.21	0.1 ± 0.2	3.99 ± 0.03	0.00 ± 0.00	-1.60 ± 0.98	1.73 ± 1.66	0.11 ± 0.99	-3.28 ± 0.02	4.31 ± 0.46	6.53 ± 0.02
UGC04426	0.48	0.06 ± 0.05	-0.6 ± 0.5	3.87 ± 0.11	0.20 ± 0.02	-1.32 ± 0.76	2.86 ± 2.12	0.98 ± 0.70	-1.87 ± 0.05	<5.52	8.06 ± 0.05
UGC04459	0.46	0.14 ± 0.05	-0.6 ± 0.5	3.86 ± 0.16	3.38 ± 2.00	-1.48 ± 0.83	0.83 ± 0.32	0.96 ± 0.28	-2.58 ± 0.10	3.81 ± 0.19	7.03 ± 0.07
UGC04483	1.12	0.05 ± 0.03	-0.8 ± 0.5	3.91 ± 0.13	3.14 ± 1.55	-0.84 ± 0.32	0.47 ± 0.00	1.58 ± 0.18	-2.82 ± 0.07	$\cdots$	6.64 ± 0.05
NGC2683	0.73	0.80 ± 0.33	-0.8 ± 0.3	3.38 ± 0.09	0.84 ± 0.60	-1.07 ± 0.56	4.39 ± 0.73	0.14 ± 0.27	-0.56 ± 0.15	7.31 ± 0.24	10.32 ± 0.05
UGC04704	2.60	0.10 ± 0.05	-0.6 ± 0.5	3.94 ± 0.08	0.21 ± 0.04	-0.61 ± 0.18	0.47 ± 0.00	1.06 ± 0.49	-1.85 ± 0.05	4.23 ± 0.39	8.00 ± 0.03
UGC04787	0.75	0.17 ± 0.06	-0.5 ± 0.5	3.84 ± 0.15	0.29 ± 0.11	-1.57 ± 1.19	1.05 ± 0.22	-0.10 ± 0.21	-2.06 ± 0.10	5.31 ± 0.24	7.96 ± 0.06
UGC04998	0.44	0.15 ± 0.09	-0.8 ± 0.5	3.30 ± 0.01	0.45 ± 0.13	-1.35 ± 0.78	4.78 ± 1.65	0.88 ± 0.79	-2.49 ± 0.12	<5.95	8.69 ± 0.02
NGC2903	0.44	1.27 ± 0.37	-0.5 ± 0.3	3.59 ± 0.19	1.16 ± 0.99	-1.56 ± 0.96	4.63 ± 0.83	0.45 ± 0.18	0.24 ± 0.09	7.66 ± 0.18	10.50 ± 0.05
UGC05076	1.52	0.08 ± 0.06	-0.7 ± 0.5	3.85 ± 0.14	0.00 ± 0.03	-1.31 ± 0.75	4.49 ± 1.76	0.98 ± 0.70	-2.23 ± 0.23	<5.37	7.91 ± 0.07
CGCG035-007	0.59	0.16 ± 0.06	-0.9 ± 0.4	3.97 ± 0.06	0.21 ± 0.03	-1.38 ± 0.79	0.91 ± 0.30	1.29 ± 0.27	-2.44 ± 0.05	3.42 ± 0.28	7.46 ± 0.03
UGC05139	0.74	0.08 ± 0.04	-0.7 ± 0.5	3.98 ± 0.05	0.40 ± 0.03	-1.82 ± 1.03	0.68 ± 0.31	0.42 ± 0.15	-2.19 ± 0.03	4.39 ± 0.19	7.61 ± 0.02
IC0559	0.82	0.10 ± 0.04	-0.8 ± 0.5	3.69 ± 0.06	0.20 ± 0.00	-1.00 ± 0.55	0.58 ± 0.24	0.79 ± 0.53	-2.38 ± 0.07	3.87 ± 0.29	7.77 ± 0.03
F8D1	1.61	0.06 ± 0.07	-0.7 ± 0.5	3.40 ± 0.12	1.10 ± 0.94	-1.32 ± 0.76	2.92 ± 2.14	0.98 ± 0.70	-2.93 ± 0.18	<4.86	7.86 ± 0.07
/FM2000/1	2.43	1.62 ± 0.72	-1.5 ± 0.0	3.94 ± 0.10	0.02 ± 0.15	-1.47 ± 0.91	1.15 ± 1.06	0.30 ± 1.47	-3.81 ± 0.40	<5.06	6.61 ± 0.08
NGC2976	0.71	0.71 ± 0.25	-0.7 ± 0.3	3.52 ± 0.12	1.38 ± 1.30	-1.45 ± 0.98	4.09 ± 0.56	0.49 ± 0.18	-1.16 ± 0.07	6.21 ± 0.15	9.18 ± 0.05
LEDA166101	1.28	0.09 ± 0.10	-0.7 ± 0.5	3.25 ± 0.13	1.23 ± 1.81	-1.28 ± 0.72	3.11 ± 2.16	0.99 ± 0.68	-3.73 ± 0.34	<4.56	7.49 ± 0.07
UGC05272	1.33	0.12 ± 0.04	-0.7 ± 0.5	3.96 ± 0.07	1.37 ± 0.22	-1.23 ± 0.57	0.47 ± 0.00	1.04 ± 0.25	-1.80 ± 0.04	4.30 ± 0.19	7.89 ± 0.03
UGC05288	0.73	0.10 ± 0.04	-0.8 ± 0.5	3.87 ± 0.12	0.61 ± 0.16	-1.72 ± 1.18	0.48 ± 0.09	0.28 ± 0.28	-1.95 ± 0.07	4.96 ± 0.25	8.01 ± 0.05
BK03N	3.81	0.05 ± 0.04	-0.5 ± 0.5	3.98 ± 0.04	0.00 ± 0.00	-1.23 ± 0.68	3.28 ± 2.18	1.02 ± 0.66	-4.10 ± 0.02	$\cdots$	5.71 ± 0.02
NGC3031	0.16	0.37 ± 0.18	-0.5 ± 0.4	3.30 ± 0.00	0.51 ± 0.14	-1.12 ± 0.61	4.17 ± 0.68	-0.04 ± 0.22	-0.41 ± 0.10	7.55 ± 0.22	10.72 ± 0.02
NGC3034	0.75	2.26 ± 0.07	-0.5 ± 0.1	3.92 ± 0.12	2.75 ± 1.45	-0.98 ± 0.28	1.70 ± 1.03	1.44 ± 0.27	0.57 ± 0.08	7.03 ± 0.62	10.09 ± 0.05
UGC05340	3.25	0.03 ± 0.01	-0.5 ± 0.5	3.99 ± 0.03	0.82 ± 0.13	-1.39 ± 0.82	2.38 ± 1.98	0.95 ± 0.73	-2.31 ± 0.02	<5.02	7.46 ± 0.02
KDG061	1.94	0.76 ± 0.17	-1.5 ± 0.1	3.67 ± 0.15	0.25 ± 0.26	-1.55 ± 0.94	0.78 ± 0.77	-0.12 ± 2.52	-3.23 ± 0.23	<5.87	7.34 ± 0.10
UGC05336	2.48	0.06 ± 0.03	-0.6 ± 0.5	3.99 ± 0.03	0.20 ± 0.01	-1.34 ± 0.83	3.93 ± 2.09	-0.01 ± 0.57	-2.45 ± 0.02	4.53 ± 0.43	7.35 ± 0.02
ArpsLoop	1.73	0.14 ± 0.18	-0.8 ± 0.5	3.59 ± 0.23	0.33 ± 0.64	-1.29 ± 0.74	2.75 ± 2.12	1.00 ± 0.68	-3.83 ± 0.34	<4.42	6.90 ± 0.13
UGC05364	2.26	0.03 ± 0.01	-0.5 ± 0.5	3.98 ± 0.04	0.20 ± 0.03	-1.37 ± 0.80	3.21 ± 2.16	0.93 ± 0.74	-3.59 ± 0.02	<3.54	6.21 ± 0.02
UGC05373	1.69	0.03 ± 0.00	-0.5 ± 0.4	3.73 ± 0.08	0.20 ± 0.00	-1.32 ± 0.45	0.85 ± 0.58	0.97 ± 0.57	-2.54 ± 0.03	$\cdots$	7.47 ± 0.03
kkh057	0.82	0.20 ± 0.25	-0.7 ± 0.5	3.44 ± 0.21	0.77 ± 0.67	-1.30 ± 0.74	2.99 ± 2.16	1.00 ± 0.67	-4.37 ± 0.27	<4.02	6.42 ± 0.08

Table 5
(Continued)

Name	$\chi^2_{\rm red}$	$A_{\rm H\alpha}$ (mag)	δ	$\log_{10}\tau_{\rm main}$ (Myr)	$\log_{10} r_{\rm SFR}$	$\log_{10}\gamma$	$q_{\rm PAH}$ (%)	$\log_{10} U_{\rm min}$	SFR$_{100}$ ($M_\odot\,{\rm yr}^{-1}$)	$\log_{10} M_{\rm dust}$ ($M_\odot$)	$\log_{10} M_*$ ($M_\odot$)
UGCA193	0.65	0.04 ± 0.01	−0.6 ± 0.5	3.83 ± 0.14	0.48 ± 0.14	−1.24 ± 0.64	1.75 ± 1.16	1.17 ± 0.51	−1.92 ± 0.10	4.35 ± 1.00	8.14 ± 0.07
NGC3109	4.61	0.10 ± 0.04	−1.0 ± 0.5	4.00 ± 0.02	0.58 ± 0.07	−1.15 ± 0.72	1.84 ± 0.69	0.52 ± 0.21	−1.83 ± 0.02	4.73 ± 0.20	7.95 ± 0.02
NGC3077	0.99	0.61 ± 0.19	−0.6 ± 0.5	3.51 ± 0.09	0.67 ± 0.35	−1.07 ± 0.63	3.61 ± 0.63	0.83 ± 0.22	−1.11 ± 0.08	5.84 ± 0.18	9.34 ± 0.04
AM1001-270	1.16	0.04 ± 0.03	−0.6 ± 0.5	3.87 ± 0.13	0.67 ± 0.44	−1.35 ± 0.78	2.92 ± 2.13	0.97 ± 0.71	−3.78 ± 0.08	<3.68	6.17 ± 0.06
BK05N	1.20	0.26 ± 0.32	−0.7 ± 0.5	3.40 ± 0.21	0.51 ± 0.62	−1.29 ± 0.73	2.97 ± 2.15	1.00 ± 0.68	−4.10 ± 0.35	<4.47	6.87 ± 0.07
UGC05428	0.72	0.16 ± 0.16	−0.7 ± 0.5	3.59 ± 0.14	0.00 ± 0.00	−1.31 ± 0.75	2.86 ± 2.13	0.98 ± 0.70	−3.40 ± 0.28	<4.64	7.21 ± 0.06
UGC05423	0.57	0.10 ± 0.05	−0.8 ± 0.5	3.90 ± 0.11	0.46 ± 0.11	−1.64 ± 0.92	1.98 ± 0.84	0.77 ± 0.24	−2.48 ± 0.09	3.96 ± 0.22	7.55 ± 0.05
UGC05442	1.97	0.05 ± 0.04	−0.8 ± 0.5	3.32 ± 0.06	0.34 ± 0.34	−1.48 ± 0.91	3.70 ± 2.03	0.82 ± 0.82	−3.63 ± 0.17	<4.36	7.52 ± 0.04
UGC05456	0.95	0.19 ± 0.06	−0.8 ± 0.5	3.96 ± 0.06	0.53 ± 0.10	−1.54 ± 0.53	0.63 ± 0.28	0.92 ± 0.24	−2.15 ± 0.06	4.17 ± 0.17	7.68 ± 0.03
SextansA	2.66	0.04 ± 0.01	−0.5 ± 0.4	3.98 ± 0.05	0.74 ± 0.14	−1.74 ± 0.84	2.21 ± 0.77	0.51 ± 0.20	−2.54 ± 0.03	3.67 ± 0.21	7.26 ± 0.02
/HS98/117	0.91	1.11 ± 0.56	−1.3 ± 0.2	3.02 ± 0.10	2.20 ± 2.70	−1.42 ± 0.86	1.32 ± 1.26	0.89 ± 0.78	−5.10 ± 1.68	<4.93	7.43 ± 0.03
NGC3239	0.65	0.20 ± 0.05	−0.9 ± 0.4	3.95 ± 0.08	1.11 ± 0.23	−1.75 ± 0.13	1.12 ± 0.05	0.66 ± 0.18	−0.72 ± 0.03	6.02 ± 0.18	9.05 ± 0.03
UGC05672	0.87	0.18 ± 0.08	−1.2 ± 0.4	3.54 ± 0.06	0.20 ± 0.01	−1.91 ± 0.92	2.40 ± 0.76	−0.34 ± 0.29	−2.40 ± 0.16	5.48 ± 0.36	8.21 ± 0.05
UGC05666	1.70	0.16 ± 0.05	−0.8 ± 0.5	3.98 ± 0.05	0.80 ± 0.13	−1.88 ± 1.02	0.66 ± 0.30	0.31 ± 0.18	−1.16 ± 0.03	5.84 ± 0.23	8.64 ± 0.02
UGC05692	0.75	0.18 ± 0.07	−0.5 ± 0.4	3.30 ± 0.01	0.49 ± 0.11	−1.10 ± 0.59	1.48 ± 0.71	0.44 ± 0.27	−2.76 ± 0.08	4.51 ± 0.25	8.34 ± 0.02
NGC3274	0.67	0.19 ± 0.06	−0.7 ± 0.5	3.94 ± 0.09	1.09 ± 0.25	−0.88 ± 0.45	2.24 ± 0.54	0.87 ± 0.23	−1.52 ± 0.03	4.98 ± 0.17	8.26 ± 0.04
BK06N	0.64	0.18 ± 0.31	−0.7 ± 0.5	3.43 ± 0.38	1.60 ± 2.27	−1.30 ± 0.74	2.63 ± 2.09	0.99 ± 0.69	−3.56 ± 0.66	<4.58	7.16 ± 0.12
NGC3299	0.30	0.24 ± 0.10	−0.7 ± 0.5	3.30 ± 0.02	1.20 ± 0.27	−1.15 ± 0.66	5.13 ± 1.00	0.02 ± 0.24	−1.83 ± 0.05	5.96 ± 0.22	9.13 ± 0.02
UGC05764	1.51	0.09 ± 0.04	−0.6 ± 0.5	3.96 ± 0.06	0.80 ± 0.13	−1.16 ± 0.67	0.83 ± 0.33	1.05 ± 0.51	−2.40 ± 0.03	3.88 ± 0.49	7.41 ± 0.03
UGC05797	0.62	0.20 ± 0.05	−1.0 ± 0.4	3.92 ± 0.08	0.20 ± 0.00	−1.14 ± 0.63	1.08 ± 0.29	0.44 ± 0.30	−2.07 ± 0.06	4.58 ± 0.28	7.88 ± 0.03
UGC05829	2.26	0.12 ± 0.04	−0.7 ± 0.5	3.98 ± 0.05	0.75 ± 0.12	−0.66 ± 0.26	0.47 ± 0.00	0.51 ± 0.19	−1.45 ± 0.03	5.09 ± 0.18	8.35 ± 0.02
NGC3344	0.26	0.62 ± 0.22	−0.3 ± 0.3	3.79 ± 0.14	0.33 ± 0.13	−1.33 ± 0.88	4.26 ± 0.73	0.16 ± 0.24	−0.41 ± 0.09	7.10 ± 0.21	9.63 ± 0.05
NGC3351	0.44	1.01 ± 0.33	−0.6 ± 0.3	3.58 ± 0.10	0.45 ± 0.24	−1.66 ± 0.13	2.62 ± 0.42	0.27 ± 0.22	−0.03 ± 0.12	7.43 ± 0.23	10.35 ± 0.04
NGC3368	0.42	0.67 ± 0.32	−0.5 ± 0.3	3.30 ± 0.00	0.40 ± 0.18	−1.34 ± 0.77	3.73 ± 0.58	0.19 ± 0.24	−0.53 ± 0.15	7.49 ± 0.24	10.66 ± 0.02
UGC05889	0.37	0.05 ± 0.04	−0.6 ± 0.5	3.53 ± 0.06	0.20 ± 0.00	−0.93 ± 0.39	1.27 ± 1.04	1.10 ± 0.61	−1.82 ± 0.09	<5.56	8.57 ± 0.05
UGC05923	0.61	0.23 ± 0.09	−1.0 ± 0.4	3.53 ± 0.10	0.38 ± 0.14	−1.18 ± 0.63	3.24 ± 0.76	1.14 ± 0.30	−2.29 ± 0.11	4.23 ± 0.21	8.23 ± 0.05
UGC05918	0.99	0.05 ± 0.04	−0.6 ± 0.5	3.72 ± 0.16	0.40 ± 0.13	−1.32 ± 0.75	2.99 ± 2.14	0.98 ± 0.70	−2.52 ± 0.13	<5.14	7.67 ± 0.06
NGC3432	0.54	0.63 ± 0.09	−0.9 ± 0.3	3.91 ± 0.10	1.30 ± 0.27	−1.04 ± 0.62	2.49 ± 0.10	0.62 ± 0.21	−0.68 ± 0.03	6.38 ± 0.18	9.08 ± 0.04
KDG073	1.75	0.17 ± 0.19	−0.4 ± 0.5	3.74 ± 0.15	0.00 ± 0.00	−1.28 ± 0.72	3.14 ± 2.17	1.00 ± 0.67	−3.54 ± 0.08	<4.22	6.54 ± 0.07
NGC3486	0.34	0.43 ± 0.14	−0.8 ± 0.4	3.90 ± 0.11	0.84 ± 0.24	−0.98 ± 0.53	4.63 ± 0.79	0.31 ± 0.25	−0.35 ± 0.05	6.90 ± 0.28	9.53 ± 0.04
NGC3510	1.11	0.25 ± 0.09	−0.8 ± 0.5	3.96 ± 0.07	0.58 ± 0.11	−1.03 ± 0.59	2.01 ± 0.66	0.62 ± 0.21	−1.33 ± 0.05	5.45 ± 0.18	8.51 ± 0.03
NGC3521	0.30	0.92 ± 0.30	−0.8 ± 0.2	3.76 ± 0.17	0.45 ± 0.36	−0.99 ± 0.53	5.85 ± 0.81	0.22 ± 0.24	0.23 ± 0.13	7.83 ± 0.25	10.47 ± 0.05
NGC3593	0.72	1.54 ± 0.25	−0.8 ± 0.1	3.76 ± 0.19	0.50 ± 0.30	−0.93 ± 0.49	4.47 ± 0.73	0.83 ± 0.21	−0.63 ± 0.12	6.42 ± 0.16	9.61 ± 0.06
NGC3623	0.65	0.22 ± 0.09	0.0 ± 0.2	3.01 ± 0.07	8.79 ± 2.10	−1.11 ± 0.61	4.10 ± 0.82	−0.23 ± 0.23	−1.69 ± 0.45	7.58 ± 0.27	10.67 ± 0.02
NGC3627	0.27	1.20 ± 0.46	−0.6 ± 0.2	3.73 ± 0.19	0.56 ± 0.59	−1.62 ± 0.97	4.05 ± 0.61	0.48 ± 0.21	0.39 ± 0.13	7.80 ± 0.24	10.63 ± 0.06
NGC3628	0.65	2.50 ± 0.12	−1.5 ± 0.1	3.87 ± 0.10	0.62 ± 0.13	−1.23 ± 0.76	4.40 ± 0.76	0.49 ± 0.23	0.37 ± 0.07	7.60 ± 0.20	10.33 ± 0.04
UGC06457	0.27	0.07 ± 0.03	−0.7 ± 0.5	3.82 ± 0.13	0.42 ± 0.10	−1.88 ± 1.13	1.04 ± 0.41	0.65 ± 0.25	−1.85 ± 0.09	4.55 ± 0.26	8.20 ± 0.05
UGC06541	0.66	0.04 ± 0.01	−0.9 ± 0.5	3.92 ± 0.10	1.62 ± 0.36	−1.83 ± 1.08	0.67 ± 0.30	1.59 ± 0.14	−2.44 ± 0.05	⋯	7.25 ± 0.04
NGC3738	0.40	0.24 ± 0.08	−0.9 ± 0.5	3.92 ± 0.07	0.39 ± 0.04	−1.03 ± 0.58	1.58 ± 0.65	0.87 ± 0.23	−1.36 ± 0.05	5.07 ± 0.17	8.51 ± 0.03
NGC3741	1.02	0.05 ± 0.02	−0.8 ± 0.5	3.96 ± 0.07	1.15 ± 0.22	−1.72 ± 1.02	0.47 ± 0.00	1.37 ± 0.18	−2.67 ± 0.03	⋯	7.08 ± 0.03
UGC06782	0.95	0.04 ± 0.03	−0.6 ± 0.5	3.82 ± 0.16	0.56 ± 0.48	−1.33 ± 0.77	2.96 ± 2.13	0.96 ± 0.71	−1.84 ± 0.10	<5.79	8.20 ± 0.07
UGC06817	2.89	0.04 ± 0.01	−0.9 ± 0.5	4.00 ± 0.02	0.40 ± 0.01	−1.20 ± 0.73	0.82 ± 0.34	0.75 ± 0.57	−2.60 ± 0.02	3.54 ± 0.38	7.18 ± 0.02
UGC06900	0.47	0.06 ± 0.06	−0.7 ± 0.5	3.38 ± 0.09	0.59 ± 0.33	−1.20 ± 0.64	4.63 ± 1.83	1.07 ± 0.62	−2.71 ± 0.15	<5.16	8.25 ± 0.05
NGC4020	0.58	0.59 ± 0.17	−0.8 ± 0.4	3.91 ± 0.11	0.42 ± 0.12	−1.38 ± 0.94	3.86 ± 0.70	0.23 ± 0.25	−1.18 ± 0.09	6.26 ± 0.22	8.77 ± 0.05
NGC4068	0.83	0.13 ± 0.05	−0.7 ± 0.5	3.96 ± 0.06	0.57 ± 0.09	−0.97 ± 0.52	0.72 ± 0.32	0.75 ± 0.23	−1.87 ± 0.05	4.49 ± 0.17	7.96 ± 0.02
NGC4080	0.49	0.44 ± 0.18	−0.6 ± 0.4	3.79 ± 0.16	0.36 ± 0.17	−1.07 ± 0.59	5.39 ± 0.85	0.04 ± 0.24	−1.83 ± 0.13	5.73 ± 0.19	8.35 ± 0.05
NGC4096	0.64	1.33 ± 0.38	−0.6 ± 0.3	3.76 ± 0.17	0.70 ± 0.38	−1.03 ± 0.55	5.18 ± 0.78	−0.00 ± 0.24	−0.43 ± 0.10	7.34 ± 0.23	9.65 ± 0.05

Table 5
(Continued)

Name	$\chi^2_{\rm red}$	$A_{\rm H\alpha}$ (mag)	δ	$\log_{10}\tau_{\rm main}$ (Myr)	$\log_{10} r_{\rm SFR}$	$\log_{10}\gamma$	$q_{\rm PAH}$ (%)	$\log_{10} U_{\rm min}$	SFR$_{100}$ ($M_\odot\,{\rm yr}^{-1}$)	$\log_{10} M_{\rm dust}$ ($M_\odot$)	$\log_{10} M_*$ ($M_\odot$)
NGC4144	0.43	0.22 ± 0.09	-0.9 ± 0.5	3.82 ± 0.14	0.51 ± 0.15	-0.96 ± 0.53	2.38 ± 0.39	0.41 ± 0.21	-0.88 ± 0.09	6.18 ± 0.21	9.19 ± 0.05
NGC4163	1.33	0.08 ± 0.03	-0.6 ± 0.5	3.62 ± 0.12	0.12 ± 0.10	-1.35 ± 0.81	0.72 ± 0.32	0.88 ± 0.44	-2.50 ± 0.10	3.56 ± 0.26	7.69 ± 0.06
NGC4190	0.72	0.11 ± 0.05	-0.7 ± 0.5	3.94 ± 0.09	0.25 ± 0.09	-1.32 ± 0.65	0.48 ± 0.08	0.79 ± 0.19	-2.08 ± 0.05	4.19 ± 0.16	7.77 ± 0.04
ESO321-G014	1.45	0.03 ± 0.01	-0.6 ± 0.5	3.87 ± 0.13	0.54 ± 0.40	-1.54 ± 0.96	0.79 ± 0.56	0.54 ± 1.00	-2.95 ± 0.09	<4.48	7.02 ± 0.06
UGC07242	3.21	0.04 ± 0.03	-0.5 ± 0.5	3.91 ± 0.11	8.95 ± 1.50	-1.35 ± 0.79	2.14 ± 1.90	0.99 ± 0.69	-2.87 ± 0.13	<4.70	6.19 ± 0.13
UGCA276	1.52	1.57 ± 0.35	-1.1 ± 0.3	3.85 ± 0.14	0.00 ± 0.00	-1.47 ± 0.90	0.80 ± 0.55	0.43 ± 1.31	-3.59 ± 0.37	<5.19	6.85 ± 0.07
UGC07267	0.69	0.08 ± 0.04	-0.6 ± 0.5	3.67 ± 0.15	0.34 ± 0.15	-0.99 ± 0.54	0.53 ± 0.19	0.29 ± 0.58	-2.18 ± 0.11	4.72 ± 0.35	8.05 ± 0.06
NGC4214	0.95	0.35 ± 0.07	-0.8 ± 0.4	3.98 ± 0.05	1.01 ± 0.13	-1.55 ± 0.14	1.21 ± 0.34	0.57 ± 0.23	-1.04 ± 0.02	5.87 ± 0.19	8.72 ± 0.02
CGCG269-049	1.79	0.06 ± 0.03	-0.9 ± 0.5	4.00 ± 0.01	0.40 ± 0.02	-0.97 ± 0.46	0.49 ± 0.12	1.56 ± 0.20	-3.07 ± 0.02	$\cdots$	6.71 ± 0.02
NGC4236	0.92	0.16 ± 0.06	-0.8 ± 0.5	3.95 ± 0.07	0.66 ± 0.12	-1.19 ± 0.76	0.89 ± 0.31	0.50 ± 0.20	-0.73 ± 0.05	5.89 ± 0.19	9.12 ± 0.03
NGC4244	0.28	0.26 ± 0.11	-0.7 ± 0.5	3.91 ± 0.11	0.24 ± 0.09	-1.45 ± 1.05	2.45 ± 0.31	0.09 ± 0.22	-0.83 ± 0.09	6.46 ± 0.18	9.14 ± 0.04
NGC4242	0.29	0.27 ± 0.11	-0.9 ± 0.4	3.91 ± 0.10	0.21 ± 0.03	-1.02 ± 0.57	2.69 ± 0.49	-0.05 ± 0.23	-0.99 ± 0.13	6.51 ± 0.23	9.09 ± 0.04
UGC07321	0.30	0.40 ± 0.20	-1.2 ± 0.3	3.87 ± 0.13	0.43 ± 0.19	-0.87 ± 0.41	2.54 ± 0.24	-0.04 ± 0.25	-0.73 ± 0.11	6.80 ± 0.20	9.29 ± 0.05
NGC4248	0.61	0.38 ± 0.15	-1.0 ± 0.4	3.47 ± 0.04	0.24 ± 0.13	-1.19 ± 0.73	4.23 ± 0.94	0.34 ± 0.23	-2.01 ± 0.19	5.45 ± 0.25	8.81 ± 0.04
NGC4258	0.27	0.42 ± 0.18	-1.1 ± 0.4	3.50 ± 0.08	0.56 ± 0.27	-1.11 ± 0.66	3.46 ± 0.72	-0.01 ± 0.21	0.15 ± 0.09	7.82 ± 0.20	10.67 ± 0.04
ISZ399	0.37	1.56 ± 0.23	-0.5 ± 0.5	3.76 ± 0.19	2.59 ± 1.51	-1.30 ± 0.18	2.51 ± 0.21	1.31 ± 0.27	-1.32 ± 0.10	5.24 ± 0.19	8.52 ± 0.07
NGC4288	0.63	0.44 ± 0.12	-0.2 ± 0.4	3.95 ± 0.07	0.63 ± 0.15	-1.14 ± 0.69	2.58 ± 0.33	0.49 ± 0.21	-1.39 ± 0.05	5.67 ± 0.18	8.44 ± 0.03
UGC07408	3.82	0.08 ± 0.06	-0.8 ± 0.4	4.00 ± 0.01	0.00 ± 0.00	-1.35 ± 0.79	2.44 ± 1.90	1.04 ± 0.64	-1.70 ± 0.02	<5.34	8.18 ± 0.02
UGC07490	0.67	0.18 ± 0.07	-0.7 ± 0.5	3.93 ± 0.08	0.21 ± 0.04	-0.93 ± 0.49	2.22 ± 0.60	-0.04 ± 0.26	-1.26 ± 0.10	5.87 ± 0.24	8.67 ± 0.04
NGC4395	2.93	0.27 ± 0.09	-1.0 ± 0.4	3.99 ± 0.02	0.35 ± 0.08	-1.30 ± 0.87	2.44 ± 0.29	0.34 ± 0.21	-0.75 ± 0.02	6.29 ± 0.26	9.03 ± 0.02
UGCA281	1.18	0.11 ± 0.05	-0.7 ± 0.5	3.80 ± 0.16	7.38 ± 2.01	-0.54 ± 0.09	0.47 ± 0.00	1.70 ± 0.02	-2.32 ± 0.14	3.42 ± 0.06	7.35 ± 0.06
UGC07559	1.31	0.07 ± 0.03	-0.6 ± 0.5	3.98 ± 0.04	0.66 ± 0.09	-1.00 ± 0.51	0.48 ± 0.06	1.36 ± 0.32	-2.23 ± 0.03	3.52 ± 0.31	7.56 ± 0.02
UGC07577	1.24	0.04 ± 0.01	-0.9 ± 0.5	3.81 ± 0.11	0.20 ± 0.00	-0.96 ± 0.48	0.47 ± 0.03	-0.14 ± 0.31	-2.32 ± 0.05	4.55 ± 0.33	7.67 ± 0.04
NGC4449	0.81	0.48 ± 0.07	-0.6 ± 0.4	3.93 ± 0.08	1.60 ± 0.29	-1.70 ± 0.97	2.50 ± 0.11	0.57 ± 0.21	-0.44 ± 0.05	6.58 ± 0.17	9.22 ± 0.04
UGC07599	1.49	0.03 ± 0.02	-0.6 ± 0.5	3.97 ± 0.05	0.20 ± 0.02	-1.36 ± 0.79	2.86 ± 2.12	0.97 ± 0.71	-2.28 ± 0.02	<4.95	7.52 ± 0.02
UGC07605	1.34	0.04 ± 0.02	-0.6 ± 0.5	3.99 ± 0.04	0.40 ± 0.02	-1.59 ± 0.98	1.54 ± 1.30	1.15 ± 0.44	-2.55 ± 0.02	<4.27	7.24 ± 0.02
NGC4455	0.37	0.18 ± 0.06	-0.6 ± 0.5	3.95 ± 0.07	0.51 ± 0.12	-1.06 ± 0.63	1.12 ± 0.06	0.30 ± 0.19	-1.35 ± 0.05	5.66 ± 0.23	8.49 ± 0.03
UGC07608	1.32	0.14 ± 0.04	-0.7 ± 0.5	3.97 ± 0.06	0.82 ± 0.13	-1.54 ± 0.73	0.93 ± 0.30	0.87 ± 0.34	-1.78 ± 0.03	4.58 ± 0.22	8.01 ± 0.02
NGC4460	0.37	0.43 ± 0.09	-1.1 ± 0.2	3.45 ± 0.08	1.17 ± 0.82	-1.73 ± 0.43	2.50 ± 0.10	0.76 ± 0.17	-1.09 ± 0.07	6.00 ± 0.15	9.41 ± 0.06
UGC07639	0.76	0.08 ± 0.04	-0.7 ± 0.5	3.80 ± 0.16	0.00 ± 0.00	-1.14 ± 0.64	0.87 ± 0.36	1.31 ± 0.35	-1.82 ± 0.07	3.91 ± 0.38	8.27 ± 0.05
NGC4485	0.74	0.44 ± 0.09	-0.8 ± 0.4	3.96 ± 0.07	1.10 ± 0.20	-1.45 ± 1.04	2.49 ± 0.14	0.19 ± 0.26	-1.10 ± 0.03	6.38 ± 0.21	8.65 ± 0.03
NGC4490	0.32	0.94 ± 0.09	-1.0 ± 0.2	3.92 ± 0.10	1.65 ± 0.40	-1.66 ± 0.96	2.50 ± 0.06	0.72 ± 0.19	0.05 ± 0.05	7.11 ± 0.18	9.73 ± 0.04
UGC07690	0.40	0.20 ± 0.06	-0.6 ± 0.5	3.95 ± 0.06	0.38 ± 0.07	-1.00 ± 0.51	1.11 ± 0.06	0.65 ± 0.21	-1.41 ± 0.04	5.17 ± 0.17	8.42 ± 0.03
UGC07699	0.72	0.19 ± 0.07	-0.7 ± 0.5	3.93 ± 0.08	0.34 ± 0.09	-1.12 ± 0.68	1.84 ± 0.69	0.47 ± 0.20	-1.44 ± 0.05	5.29 ± 0.24	8.41 ± 0.03
UGC07698	0.51	0.09 ± 0.04	-0.7 ± 0.5	3.97 ± 0.06	0.63 ± 0.09	-1.22 ± 0.70	4.77 ± 0.99	0.60 ± 0.27	-1.78 ± 0.05	4.71 ± 0.23	8.04 ± 0.03
UGC07719	0.52	0.17 ± 0.06	-0.7 ± 0.5	3.95 ± 0.07	0.60 ± 0.11	-1.05 ± 0.46	0.47 ± 0.00	1.60 ± 0.15	-1.84 ± 0.05	3.80 ± 0.19	8.00 ± 0.03
UGC07774	0.42	0.17 ± 0.06	-0.7 ± 0.5	3.90 ± 0.12	0.24 ± 0.09	-1.81 ± 1.12	1.20 ± 0.47	0.23 ± 0.29	-1.95 ± 0.11	5.03 ± 0.23	8.07 ± 0.05
UGCA292	0.81	0.06 ± 0.03	-0.7 ± 0.5	3.79 ± 0.16	6.57 ± 1.81	-1.47 ± 0.90	4.58 ± 1.22	1.16 ± 0.47	-3.09 ± 0.07	<4.10	6.16 ± 0.09
NGC4594	1.74	0.82 ± 0.07	-1.4 ± 0.1	3.48 ± 0.01	0.00 ± 0.00	-1.06 ± 0.57	1.47 ± 0.81	-0.62 ± 0.24	-1.32 ± 1.80	8.08 ± 0.22	10.95 ± 0.02
NGC4605	0.61	0.72 ± 0.21	-0.8 ± 0.3	3.78 ± 0.17	0.83 ± 0.40	-0.96 ± 0.48	3.74 ± 0.48	0.64 ± 0.22	-0.70 ± 0.07	6.39 ± 0.18	9.33 ± 0.06
NGC4618	0.46	0.42 ± 0.15	-0.6 ± 0.5	3.96 ± 0.06	0.48 ± 0.11	-1.09 ± 0.60	3.98 ± 0.53	0.48 ± 0.23	-0.56 ± 0.05	6.50 ± 0.20	9.26 ± 0.03
NGC4625	0.23	0.55 ± 0.22	-0.2 ± 0.3	3.92 ± 0.09	0.34 ± 0.12	-1.01 ± 0.55	5.42 ± 0.76	0.29 ± 0.22	-1.01 ± 0.06	6.25 ± 0.24	8.87 ± 0.04
NGC4631	0.43	1.36 ± 0.15	-0.5 ± 0.2	3.90 ± 0.11	2.01 ± 0.71	-1.04 ± 0.59	4.12 ± 0.55	0.62 ± 0.24	0.38 ± 0.07	7.58 ± 0.22	10.07 ± 0.05
UGC07866	1.47	0.05 ± 0.02	-0.8 ± 0.5	3.96 ± 0.07	0.91 ± 0.16	-1.76 ± 0.96	0.52 ± 0.18	0.97 ± 0.19	-2.15 ± 0.03	3.86 ± 0.18	7.65 ± 0.03
NGC4656	2.78	0.22 ± 0.04	-0.8 ± 0.4	3.97 ± 0.05	1.94 ± 0.24	-0.70 ± 0.30	0.93 ± 0.30	0.84 ± 0.25	-0.41 ± 0.05	6.06 ± 0.19	9.11 ± 0.02
UGC07916	0.56	0.08 ± 0.03	-0.7 ± 0.5	3.92 ± 0.10	1.32 ± 0.29	-1.26 ± 0.78	0.53 ± 0.18	0.81 ± 0.45	-1.93 ± 0.04	4.35 ± 0.26	7.82 ± 0.04
UGC07950	0.86	0.16 ± 0.05	-0.5 ± 0.5	3.79 ± 0.11	0.20 ± 0.00	-1.00 ± 0.50	0.74 ± 0.32	0.71 ± 0.28	-1.64 ± 0.04	4.72 ± 0.19	8.33 ± 0.05

Table 5
(Continued)

Name	$\chi^2_{\rm red}$	$A_{\rm H\alpha}$ (mag)	δ	$\log_{10} \tau_{\rm main}$ (Myr)	$\log_{10} r_{\rm SFR}$	$\log_{10} \gamma$	$q_{\rm PAH}$ (%)	$\log_{10} U_{\rm min}$	SFR$_{100}$ ($M_\odot{\rm yr}^{-1}$)	$\log_{10} M_{\rm dust}$ ($M_\odot$)	$\log_{10} M_*$ ($M_\odot$)
UGC07949	2.30	0.04 ± 0.03	−0.5 ± 0.5	3.98 ± 0.05	0.38 ± 0.05	−1.20 ± 0.62	3.34 ± 2.23	1.18 ± 0.54	−1.99 ± 0.02	<5.30	7.81 ± 0.02
NGC4707	1.00	0.11 ± 0.05	−0.6 ± 0.5	3.98 ± 0.05	0.41 ± 0.05	−1.15 ± 0.71	1.01 ± 0.24	0.46 ± 0.27	−1.73 ± 0.03	4.88 ± 0.24	8.07 ± 0.02
NGC4736	0.54	0.81 ± 0.23	0.0 ± 0.2	3.30 ± 0.01	0.72 ± 0.21	−0.96 ± 0.49	4.59 ± 0.78	0.72 ± 0.24	−0.61 ± 0.06	6.86 ± 0.18	10.44 ± 0.02
UGC08024	2.33	0.03 ± 0.01	−0.5 ± 0.5	4.00 ± 0.02	0.40 ± 0.02	−1.36 ± 0.79	2.95 ± 2.13	0.96 ± 0.72	−2.38 ± 0.02	<4.83	7.40 ± 0.02
NGC4826	0.50	0.73 ± 0.23	−1.2 ± 0.2	3.47 ± 0.04	0.27 ± 0.24	−1.00 ± 0.51	3.45 ± 0.71	0.68 ± 0.22	−0.09 ± 0.17	7.02 ± 0.18	10.67 ± 0.03
UGC08091	0.42	0.04 ± 0.01	−0.5 ± 0.4	3.94 ± 0.08	2.08 ± 0.46	−1.03 ± 0.56	0.57 ± 0.24	0.62 ± 0.48	−3.01 ± 0.06	3.23 ± 0.30	6.54 ± 0.04
UGCA319	0.90	0.05 ± 0.03	−0.7 ± 0.5	3.94 ± 0.08	0.00 ± 0.00	−1.37 ± 0.80	5.25 ± 1.44	0.88 ± 0.80	−2.02 ± 0.04	<5.40	7.89 ± 0.04
UGCA320	4.18	0.05 ± 0.02	−0.9 ± 0.5	3.98 ± 0.05	1.43 ± 0.21	−0.88 ± 0.38	0.47 ± 0.00	1.20 ± 0.35	−1.43 ± 0.04	4.43 ± 0.23	8.21 ± 0.03
UGC08188	0.80	0.12 ± 0.05	−0.6 ± 0.5	3.98 ± 0.05	0.22 ± 0.06	−1.04 ± 0.60	1.38 ± 0.55	0.55 ± 0.24	−1.37 ± 0.03	5.14 ± 0.19	8.44 ± 0.02
UGC08201	1.98	0.03 ± 0.01	−0.7 ± 0.5	4.00 ± 0.02	0.00 ± 0.01	−1.35 ± 0.76	0.74 ± 0.36	0.81 ± 0.36	−1.91 ± 0.02	3.93 ± 0.30	7.89 ± 0.02
MCG-03-34-002	0.71	0.09 ± 0.05	−0.8 ± 0.5	3.90 ± 0.11	0.22 ± 0.15	−1.03 ± 0.56	0.84 ± 0.33	1.27 ± 0.35	−1.75 ± 0.14	4.06 ± 0.28	8.32 ± 0.05
UGC08245	1.02	0.12 ± 0.06	−0.7 ± 0.5	3.82 ± 0.15	0.00 ± 0.02	−0.96 ± 0.50	0.73 ± 0.32	0.29 ± 0.40	−2.59 ± 0.08	4.18 ± 0.30	7.50 ± 0.06
NGC5023	0.55	0.17 ± 0.07	−0.8 ± 0.5	3.88 ± 0.13	0.28 ± 0.11	−1.48 ± 1.05	2.16 ± 0.60	0.38 ± 0.22	−1.57 ± 0.11	5.37 ± 0.25	8.49 ± 0.05
CGCG217-018	0.35	0.16 ± 0.06	−0.8 ± 0.5	3.91 ± 0.11	0.25 ± 0.09	−1.41 ± 0.83	1.28 ± 0.55	0.93 ± 0.32	−2.03 ± 0.13	4.31 ± 0.21	8.07 ± 0.04
UGC08313	1.07	0.13 ± 0.05	−1.0 ± 0.4	3.63 ± 0.17	1.04 ± 0.56	−1.49 ± 0.08	1.04 ± 0.27	0.56 ± 0.24	−1.93 ± 0.06	4.87 ± 0.21	8.28 ± 0.06
UGC08320	1.28	0.09 ± 0.04	−0.9 ± 0.5	3.99 ± 0.03	0.20 ± 0.01	−1.22 ± 0.58	0.47 ± 0.04	0.76 ± 0.24	−1.83 ± 0.02	4.43 ± 0.21	7.97 ± 0.02
UGC08331	1.02	0.17 ± 0.06	−0.4 ± 0.5	3.98 ± 0.05	0.20 ± 0.00	−1.05 ± 0.61	0.53 ± 0.19	0.32 ± 0.32	−1.83 ± 0.02	5.02 ± 0.27	7.98 ± 0.02
NGC5055	0.26	1.09 ± 0.44	−0.4 ± 0.3	3.60 ± 0.12	0.43 ± 0.32	−1.09 ± 0.62	4.90 ± 0.83	−0.02 ± 0.23	0.15 ± 0.14	8.10 ± 0.24	10.54 ± 0.05
NGC5068	0.50	0.31 ± 0.12	−1.1 ± 0.3	3.94 ± 0.08	0.77 ± 0.17	−1.03 ± 0.57	4.63 ± 0.77	0.35 ± 0.24	−0.34 ± 0.04	6.92 ± 0.27	9.51 ± 0.03
IC4247	1.65	0.08 ± 0.03	−0.6 ± 0.4	3.67 ± 0.05	0.20 ± 0.01	−1.00 ± 0.55	0.54 ± 0.21	0.84 ± 0.55	−2.39 ± 0.03	3.74 ± 0.31	7.68 ± 0.04
NGC5204	0.81	0.22 ± 0.06	−0.9 ± 0.5	3.97 ± 0.06	0.87 ± 0.14	−0.96 ± 0.52	2.19 ± 0.58	0.60 ± 0.23	−1.31 ± 0.03	5.49 ± 0.20	8.48 ± 0.02
NGC5194	1.20	1.40 ± 0.20	−0.4 ± 0.2	3.78 ± 0.16	1.05 ± 0.51	−1.02 ± 0.58	4.60 ± 0.82	0.23 ± 0.30	0.58 ± 0.06	8.20 ± 0.27	10.55 ± 0.06
NGC5195	1.98	0.32 ± 0.16	0.0 ± 0.2	3.00 ± 0.04	2.80 ± 2.59	−1.46 ± 0.11	1.10 ± 0.52	0.75 ± 0.20	−2.41 ± 0.69	6.21 ± 0.17	10.48 ± 0.02
UGC08508	0.53	0.07 ± 0.03	−0.6 ± 0.5	3.97 ± 0.06	0.41 ± 0.04	−1.03 ± 0.54	1.60 ± 0.70	0.86 ± 0.40	−2.71 ± 0.06	3.39 ± 0.23	7.13 ± 0.03
NGC5229	0.51	0.19 ± 0.06	−0.9 ± 0.4	3.83 ± 0.11	0.42 ± 0.08	−0.96 ± 0.49	1.04 ± 0.22	0.63 ± 0.26	−2.06 ± 0.09	4.51 ± 0.19	8.01 ± 0.05
NGC5238	1.19	0.13 ± 0.06	−0.9 ± 0.5	3.94 ± 0.08	0.64 ± 0.12	−1.08 ± 0.56	0.50 ± 0.13	0.49 ± 0.25	−1.92 ± 0.06	4.76 ± 0.22	7.98 ± 0.03
[KK98]208	9.85	0.06 ± 0.06	−0.8 ± 0.5	3.95 ± 0.08	0.09 ± 0.16	−1.31 ± 0.75	2.30 ± 2.00	1.01 ± 0.67	−3.07 ± 0.22	<4.58	7.07 ± 0.05
NGC5236	0.24	1.20 ± 0.14	−0.8 ± 0.2	3.91 ± 0.10	0.82 ± 0.22	−1.69 ± 0.37	4.09 ± 0.56	0.50 ± 0.20	0.49 ± 0.04	7.67 ± 0.18	10.37 ± 0.04
ESO444-G084	1.31	0.04 ± 0.02	−0.7 ± 0.5	3.97 ± 0.06	0.68 ± 0.14	−1.23 ± 0.68	0.48 ± 0.06	1.20 ± 0.37	−2.59 ± 0.04	3.25 ± 0.37	7.22 ± 0.03
UGC08638	0.51	0.09 ± 0.04	−0.6 ± 0.5	3.80 ± 0.15	0.59 ± 0.18	−1.31 ± 0.84	0.49 ± 0.12	0.70 ± 0.44	−2.52 ± 0.08	3.97 ± 0.26	7.53 ± 0.06
UGC08651	0.60	0.04 ± 0.01	−0.7 ± 0.5	3.95 ± 0.07	0.54 ± 0.11	−0.97 ± 0.48	0.48 ± 0.06	0.96 ± 0.55	−2.74 ± 0.05	3.37 ± 0.46	7.09 ± 0.03
NGC5253	0.38	0.53 ± 0.14	−0.8 ± 0.4	3.92 ± 0.10	2.34 ± 1.12	−0.67 ± 0.13	0.55 ± 0.21	0.92 ± 0.34	−1.02 ± 0.08	5.45 ± 0.22	8.61 ± 0.05
NGC5264	1.31	0.19 ± 0.06	−0.7 ± 0.5	3.59 ± 0.06	0.22 ± 0.06	−1.32 ± 0.85	4.16 ± 1.05	0.28 ± 0.28	−1.91 ± 0.15	5.26 ± 0.29	8.53 ± 0.04
UGC08760	0.87	0.03 ± 0.01	−0.6 ± 0.5	3.97 ± 0.06	0.20 ± 0.01	−1.45 ± 0.90	0.77 ± 0.49	0.93 ± 0.72	−2.70 ± 0.02	<4.61	7.11 ± 0.02
kkh086	3.93	0.15 ± 0.13	−0.8 ± 0.5	3.88 ± 0.13	0.13 ± 0.21	−1.22 ± 0.66	3.29 ± 2.15	1.00 ± 0.68	−4.12 ± 0.22	<3.91	6.10 ± 0.06
UGC08837	1.11	0.12 ± 0.05	−0.7 ± 0.5	3.91 ± 0.10	0.42 ± 0.07	−1.80 ± 1.13	1.43 ± 0.61	0.18 ± 0.28	−1.54 ± 0.10	5.47 ± 0.22	8.40 ± 0.05
UGC08833	2.26	0.04 ± 0.02	−0.6 ± 0.5	3.99 ± 0.04	0.20 ± 0.01	−1.27 ± 0.71	3.17 ± 2.16	1.00 ± 0.68	−3.07 ± 0.02	<4.15	6.73 ± 0.02
NGC5457	0.42	0.71 ± 0.18	−0.1 ± 0.2	3.89 ± 0.11	0.58 ± 0.26	−1.80 ± 1.10	3.82 ± 0.53	0.11 ± 0.23	0.46 ± 0.07	8.05 ± 0.17	10.36 ± 0.05
NGC5474	0.44	0.22 ± 0.09	−0.5 ± 0.5	3.91 ± 0.09	0.36 ± 0.10	−0.83 ± 0.41	2.43 ± 0.32	0.28 ± 0.26	−0.78 ± 0.06	6.28 ± 0.25	9.10 ± 0.04
NGC5477	0.64	0.14 ± 0.05	−0.6 ± 0.5	3.94 ± 0.09	1.09 ± 0.24	−0.84 ± 0.34	0.47 ± 0.00	0.98 ± 0.31	−1.73 ± 0.03	4.53 ± 0.20	8.06 ± 0.04
[KK98]230	1.25	0.04 ± 0.03	−0.6 ± 0.5	3.99 ± 0.03	0.00 ± 0.00	−1.25 ± 0.69	3.13 ± 2.17	1.02 ± 0.66	−4.06 ± 0.02	⋯	5.74 ± 0.02
UGC09128	1.37	0.03 ± 0.01	−0.6 ± 0.5	3.99 ± 0.02	0.00 ± 0.00	−1.36 ± 0.79	2.48 ± 2.02	0.97 ± 0.70	−3.10 ± 0.02	<3.99	6.70 ± 0.02
NGC5585	2.02	0.20 ± 0.07	−1.0 ± 0.4	3.99 ± 0.03	0.43 ± 0.07	−0.96 ± 0.51	2.51 ± 0.15	0.39 ± 0.23	−1.06 ± 0.02	5.89 ± 0.23	8.73 ± 0.02
UGC09240	0.88	0.14 ± 0.04	−0.6 ± 0.5	3.86 ± 0.09	0.20 ± 0.00	−1.45 ± 0.90	0.89 ± 0.31	0.74 ± 0.28	−2.38 ± 0.04	3.88 ± 0.20	7.52 ± 0.05
UGC09405	0.95	0.14 ± 0.06	−0.7 ± 0.5	3.90 ± 0.11	0.00 ± 0.00	−1.52 ± 0.93	2.68 ± 1.04	0.36 ± 0.88	−1.98 ± 0.04	4.92 ± 0.54	7.97 ± 0.04
MRK475	1.50	0.09 ± 0.03	−0.9 ± 0.5	3.56 ± 0.14	7.92 ± 2.35	−1.10 ± 0.59	0.50 ± 0.14	1.67 ± 0.08	−2.71 ± 0.07	3.35 ± 0.11	7.35 ± 0.06
NGC5832	0.30	0.22 ± 0.10	−0.6 ± 0.5	3.87 ± 0.12	0.23 ± 0.07	−0.97 ± 0.50	3.12 ± 0.73	0.06 ± 0.28	−1.11 ± 0.10	6.17 ± 0.23	8.93 ± 0.05

Table 5
(Continued)

Name	$\chi^2_{\rm red}$	$A_{\rm H\alpha}$ (mag)	δ	$\log_{10} \tau_{\rm main}$ (Myr)	$\log_{10} r_{\rm SFR}$	$\log_{10} \gamma$	$q_{\rm PAH}$ (%)	$\log_{10} U_{\rm min}$	SFR_{100} ($M_\odot\,\mathrm{yr}^{-1}$)	$\log_{10} M_{\rm dust}$ ($M_\odot$)	$\log_{10} M_*$ ($M_\odot$)
NGC5949	0.24	0.70 ± 0.21	−0.8 ± 0.3	3.62 ± 0.17	0.66 ± 0.30	−1.00 ± 0.53	5.52 ± 0.76	0.26 ± 0.24	−1.20 ± 0.09	6.35 ± 0.25	9.11 ± 0.05
UGC09992	1.22	0.13 ± 0.05	−0.6 ± 0.5	3.95 ± 0.08	0.21 ± 0.05	−1.12 ± 0.65	1.29 ± 0.59	1.05 ± 0.43	−1.96 ± 0.04	4.16 ± 0.28	7.88 ± 0.04
KKR25	2.95	0.08 ± 0.08	−0.8 ± 0.5	3.91 ± 0.11	0.01 ± 0.08	−1.29 ± 0.73	2.72 ± 2.11	1.01 ± 0.67	−4.57 ± 0.47	⋯	6.08 ± 0.06
NGC6503	0.50	0.72 ± 0.22	−0.9 ± 0.3	3.69 ± 0.16	0.60 ± 0.29	−1.26 ± 0.75	5.10 ± 0.72	0.39 ± 0.18	−0.69 ± 0.09	6.59 ± 0.21	9.50 ± 0.05
IC4951	0.77	0.08 ± 0.04	−0.7 ± 0.5	3.95 ± 0.07	0.55 ± 0.11	−0.91 ± 0.43	0.48 ± 0.08	0.84 ± 0.35	−1.45 ± 0.05	4.64 ± 0.21	8.39 ± 0.03
DDO210	1.30	0.04 ± 0.02	−0.6 ± 0.5	3.97 ± 0.05	0.00 ± 0.00	−1.35 ± 0.79	2.60 ± 2.06	0.97 ± 0.70	−3.93 ± 0.02	⋯	5.89 ± 0.02
IC5052	0.69	0.27 ± 0.10	−0.7 ± 0.5	3.63 ± 0.15	1.06 ± 0.51	−1.73 ± 0.16	1.88 ± 0.69	0.55 ± 0.21	−1.15 ± 0.06	5.87 ± 0.18	9.01 ± 0.06
NGC7064	0.46	0.11 ± 0.05	−0.7 ± 0.5	3.79 ± 0.16	1.55 ± 1.02	−1.28 ± 0.61	1.09 ± 0.13	0.83 ± 0.21	−1.15 ± 0.06	5.33 ± 0.18	8.74 ± 0.06
NGC7090	0.36	0.77 ± 0.24	−1.0 ± 0.3	3.81 ± 0.16	0.71 ± 0.36	−1.01 ± 0.57	3.58 ± 0.62	0.35 ± 0.23	−0.31 ± 0.08	7.06 ± 0.25	9.72 ± 0.06
IC5152	0.77	0.18 ± 0.06	−0.6 ± 0.5	3.93 ± 0.10	0.46 ± 0.15	−0.87 ± 0.44	2.49 ± 0.27	0.30 ± 0.24	−1.74 ± 0.08	5.23 ± 0.23	8.15 ± 0.04
IC5256	1.15	0.32 ± 0.17	−1.1 ± 0.4	3.66 ± 0.17	0.92 ± 0.55	−1.12 ± 0.64	4.67 ± 0.85	0.46 ± 0.21	−1.71 ± 0.09	5.38 ± 0.19	8.46 ± 0.07
UGCA438	1.42	0.04 ± 0.02	−0.5 ± 0.5	3.93 ± 0.08	0.00 ± 0.00	−1.31 ± 0.74	3.85 ± 1.95	0.99 ± 0.69	−2.84 ± 0.03	<4.19	7.02 ± 0.04
ESO347-G017	0.67	0.12 ± 0.05	−0.7 ± 0.5	3.92 ± 0.09	0.59 ± 0.14	−1.49 ± 0.79	0.53 ± 0.19	1.10 ± 0.25	−1.66 ± 0.06	4.44 ± 0.21	8.23 ± 0.05
UGC12613	0.99	0.16 ± 0.06	−1.1 ± 0.4	3.78 ± 0.13	0.00 ± 0.00	−1.62 ± 1.16	2.17 ± 0.88	−0.01 ± 0.23	−4.01 ± 0.55	3.74 ± 0.21	6.90 ± 0.05
IC5332	1.12	0.28 ± 0.11	−0.6 ± 0.5	3.84 ± 0.13	0.43 ± 0.13	−1.26 ± 0.82	3.39 ± 0.72	−0.11 ± 0.21	−0.35 ± 0.10	7.22 ± 0.24	9.65 ± 0.06
NGC7713	0.57	0.36 ± 0.14	−0.8 ± 0.5	3.88 ± 0.13	0.68 ± 0.27	−1.05 ± 0.61	2.49 ± 0.13	0.54 ± 0.22	−0.69 ± 0.08	6.37 ± 0.19	9.25 ± 0.06
UGCA442	0.91	0.04 ± 0.02	−0.7 ± 0.5	3.97 ± 0.05	0.43 ± 0.07	−1.68 ± 0.78	0.48 ± 0.06	0.43 ± 0.55	−2.20 ± 0.04	4.28 ± 0.35	7.61 ± 0.02
kkh098	1.27	0.05 ± 0.04	−0.7 ± 0.5	3.92 ± 0.10	0.46 ± 0.24	−1.35 ± 0.79	2.76 ± 2.09	0.95 ± 0.72	−3.38 ± 0.09	<4.25	6.56 ± 0.04
ESO149-G003	2.21	0.04 ± 0.01	−0.6 ± 0.5	3.97 ± 0.06	0.83 ± 0.14	−1.89 ± 1.19	0.50 ± 0.13	0.79 ± 0.47	−2.35 ± 0.03	<4.52	7.44 ± 0.03
NGC7793	0.54	0.44 ± 0.15	−0.5 ± 0.4	3.86 ± 0.13	0.85 ± 0.34	−0.90 ± 0.45	4.01 ± 0.52	0.09 ± 0.29	−0.52 ± 0.06	7.02 ± 0.24	9.39 ± 0.05

(This table is available in machine-readable form.)

Appendix

Table 4 provides the photometry corrected for neither Galactic nor intrinsic extinction. 5σ upper limits are included where available. The fit values are found in Table 5. Best-fit values are presented for χ^2_{reduced} and Bayesian-fit values and their corresponding uncertainties are presented for the remaining parameters. SFR_{100} is the star-formation rate averaged over

the past 100 Myr. Masses assume the distances presented in Dale et al. (2009).

ORCID iDs

Daniel A. Dale ⬤ https://orcid.org/0000-0002-5782-9093
Médéric Boquien ⬤ https://orcid.org/0000-0003-0946-6176
Jordan A. Turner ⬤ https://orcid.org/0000-0003-2261-5746
Daniela Calzetti ⬤ https://orcid.org/0000-0002-5189-8004
Robert C. Kennicutt, Jr. ⬤ https://orcid.org/0000-0001-5448-1821
Janice C. Lee ⬤ https://orcid.org/0000-0002-2278-9407

References

Armus, L., Mazzarella, J. M., Evans, A. S., et al. 2009, PASP, 121, 559
Berg, D. A., Skillman, E. D., Marble, A. R., et al. 2012, ApJ, 754, 98
Bergvall, N., Marquart, T., Way, M. J., et al. 2016, A&A, 587, A72
Boquien, M., Bendo, G., Calzetti, D., et al. 2010, ApJ, 713, 626
Boquien, M., Buat, V., Boselli, A., et al. 2012, A&A, 539, A145
Boquien, M., Burgarella, D., Roehlly, Y., et al. 2019, A&A, 622, A103
Bothwell, M. S., Kennicutt, R. C., Johnson, B. D., et al. 2011, MNRAS, 415, 1815
Bruzual, G., & Charlot, S. 2003, MNRAS, 344, 1000
Calzetti, D., Armus, L., Bohlin, R. C., et al. 2000, ApJ, 533, 682
Calzetti, D., Wu, S. Y., Hong, S., et al. 2010, ApJ, 714, 1256
Chabrier, G. 2003, PASP, 115, 763
Chastenet, J., Sandstrom, K., Chiang, I.-D., et al. 2019, ApJ, 876, 62
Cook, D. O., Dale, D. A., Johnson, B. D., et al. 2014a, MNRAS, 445, 899
Cook, D. O., Dale, D. A., Johnson, B. D., et al. 2014b, MNRAS, 445, 881
Cook, D. O., Dale, D. A., Lee, J. C., et al. 2016, MNRAS, 462, 3766
da Cunha, E., Charlot, S., & Elbaz, D. 2008, MNRAS, 388, 1595
Dalcanton, J. J., Williams, B. F., Seth, A. C., et al. 2009, ApJS, 183, 67
Dale, D. A., Aniano, G., Engelbracht, C. W., et al. 2012, ApJ, 745, 95
Dale, D. A., Beltz-Mohrmann, G. D., Egan, A. A., et al. 2016, AJ, 151, 4
Dale, D. A., Boquien, M., Barnes, A. T., et al. 2023, ApJL, 944, L23
Dale, D. A., Cohen, S. A., Johnson, L. C., et al. 2009, ApJ, 703, 517
Dale, D. A., Cook, D. O., Roussel, H., et al. 2017, ApJ, 837, 90
Dale, D. A., Gil de Paz, A., Gordon, K. D., et al. 2007, ApJ, 655, 863
Dale, D. A., Helou, G., Contursi, A., Silbermann, N. A., & Kolhatkar, S. 2001, ApJ, 549, 215
Dale, D. A., Helou, G., Magdis, G. E., et al. 2014, ApJ, 784, 83
Draine, B. T. 2003, ARA&A, 41, 241
Draine, B. T., Aniano, G., Krause, O., et al. 2014, ApJ, 780, 172
Draine, B. T., Dale, D. A., Bendo, G., et al. 2007, ApJ, 663, 866
Engelbracht, C. W., Gordon, K. D., Rieke, G. H., et al. 2005, ApJL, 628, L29
Engelbracht, C. W., Rieke, G. H., Gordon, K. D., et al. 2008, ApJ, 678, 804
Galliano, F., Nersesian, A., Bianchi, S., et al. 2021, A&A, 649, A18
Gil de Paz, A., Madore, B. F., & Pevunova, O. 2003, ApJS, 147, 29
Giovannoli, E., Buat, V., Noll, S., Burgarella, D., & Magnelli, B. 2011, A&A, 525, A150
Grasha, K., Calzetti, D., Andrews, J. E., Lee, J. C., & Dale, D. A. 2013, ApJ, 773, 174
Hao, C.-N., Kennicutt, R. C., Johnson, B. D., et al. 2011, ApJ, 741, 124
Herrera-Camus, R., Sturm, E., Graciá-Carpio, J., et al. 2018, ApJ, 861, 94
Hunt, L. K., De Looze, I., Boquien, M., et al. 2019, A&A, 621, A51
Janowiecki, S., Salzer, J. J., van Zee, L., Rosenberg, J. L., & Skillman, E. 2017, ApJ, 836, 128
Kennicutt, R. C., Calzetti, D., Aniano, G., et al. 2011, PASP, 123, 1347
Kennicutt, R. C., & Evans, N. J. 2012, ARA&A, 50, 531
Kennicutt, R. C. J., Armus, L., Bendo, G., et al. 2003, PASP, 115, 928
Kennicutt, R. C. J., Hao, C.-N., Calzetti, D., et al. 2009, ApJ, 703, 1672
Kennicutt, R. C. J., Lee, J. C., Funes, J. G., et al. 2008, ApJS, 178, 247
Kirby, E. N., Cohen, J. G., Guhathakurta, P., et al. 2013, ApJ, 779, 102
Lee, H., Skillman, E. D., Cannon, J. M., et al. 2006, ApJ, 647, 970
Lee, J. C., Gil de Paz, A., Kennicutt, R. C. J., et al. 2011, ApJS, 192, 6
Lee, J. C., Kennicutt, R. C. J., Funes, S. J. J. G., Sakai, S., & Akiyama, S. 2009a, ApJ, 692, 1305
Lee, J. C., Gil de Paz, A., Tremonti, C., et al. 2009b, ApJ, 706, 599
Leitherer, C., Li, I. H., Calzetti, D., & Heckman, T. M. 2002, ApJS, 140, 303
Leja, J., Johnson, B. D., Conroy, C., van Dokkum, P. G., & Byler, N. 2017, ApJ, 837, 170
Leroy, A. K., Sandstrom, K. M., Lang, D., et al. 2019, ApJS, 244, 24
Madden, S. C., Galliano, F., Jones, A. P., & Sauvage, M. 2006, A&A, 446, 877

Madden, S. C., Rémy-Ruyer, A., Galametz, M., et al. 2013, PASP, 125, 600
Marble, A. R., Engelbracht, C. W., van Zee, L., et al. 2010, ApJ, 715, 506
McGaugh, S. S., & Schombert, J. M. 2014, AJ, 148, 77
Meidt, S. E., Schinnerer, E., van de Ven, G., et al. 2014, ApJ, 788, 144
Moshir, M., et al. 1990, IRAS Faint Source Catalogue, v2.0
Peng, Y.-j., Lilly, S. J., Kovač, K., et al. 2010, ApJ, 721, 193
Rémy-Ruyer, A., Madden, S. C., Galliano, F., et al. 2015, A&A, 582, A121
Rice, W., Lonsdale, C. J., Soifer, B. T., et al. 1988, ApJS, 68, 91
Salim, S., Lee, J. C., Janowiecki, S., et al. 2016, ApJS, 227, 2
Salim, S., & Narayanan, D. 2020, ARA&A, 58, 529

Sanders, D. B., Mazzarella, J. M., Kim, D. C., Surace, J. A., & Soifer, B. T.
    2003, AJ, 126, 1607
Sandstrom, K. M., Bolatto, A. D., Draine, B. T., Bot, C., & Stanimirović, S.
    2010, ApJ, 715, 701
Sawicki, M. 2012, PASP, 124, 1208
Sheth, K., Regan, M., Hinz, J. L., et al. 2010, PASP, 122, 1397
Taylor, E. N., Hopkins, A. M., Baldry, I. K., et al. 2011, MNRAS, 418, 1587
Tremonti, C. A., Heckman, T. M., Kauffmann, G., et al. 2004, ApJ, 613, 898
Weisz, D. R., Johnson, B. D., Johnson, L. C., et al. 2012, ApJ, 744, 44
Wu, Y., Charmandaris, V., Hao, L., et al. 2006, ApJ, 639, 157
Wu, Y., Helou, G., Armus, L., et al. 2010, ApJ, 723, 895